Nano Research

Open Access

Research Article

PDE4B selective inhibitor unveils novel therapeutic avenue by targeting inflammation and cellular senescence in chronic obstructive pulmonary disease

Hao Ren[1,§], Chenguang Guo[1,§], Chao Teng[2], Qihao Dai[1], Ruijian Sun[1], Ruitao Zhang[3], Jianing Ma[3], Zhengjie Meng[4], Xueming Li[1] ✉, and Qiyue Wang[1,2,3] ✉

[1] *School of Pharmaceutical Science, Nanjing Tech University, Nanjing 211816, China*
[2] *Fujian Key Laboratory of Natural Medicine Pharmacology, School of Pharmacy, Fujian Medical University, Fuzhou 350122, China*
[3] *NMPA Key Laboratory for Research and Evaluation of Pharmaceutical Preparation and Excipients, China Pharmaceutical University, Nanjing 210009, China*
[4] *College of Biotechnology and Pharmaceutical Engineering, Nanjing Tech University, Nanjing 211816, China*
[§] *Hao Ren and Chenguang Guo contributed equally to this work.*

Cite this article: *Nano Research*, **2026**, *19*, 94908499. https://doi.org/10.26599/NR.2026.94908499

ABSTRACT: Chronic obstructive pulmonary disease (COPD), a respiratory disorder characterized by airway remodeling within a chronic inflammatory microenvironment, affects millions worldwide. Cigarette smoke, the primary etiological factor, triggers chronic pulmonary inflammation and respiratory epithelial cell senescence, rendering anti-inflammatory strategies pivotal for alleviating COPD progression and pulmonary aging. This study demonstrates that A33, a highly selective phosphodiesterase 4B inhibitor, potently attenuates chronic inflammation by suppressing nuclear factor kappa-B (NF-κB) activation in damaged epithelial cells and reducing the secretion of pro-inflammatory cytokines. Additionally, A33 exhibits senolytic potential by regulating the senescence-associated secretory phenotype (SASP) in senescent cells. A33 encapsulated liposomes decorated with mPEG (incorporating 5% DSPE-mPEG in the formulations) exhibited satisfactory stability and enhanced respiratory mucus penetration ability, successfully improving the effective pulmonary epithelial delivery of A33. Both *in vitro* and *in vivo* experiments show that mPEG-decorated A33-encapsulated liposomes enhance pulmonary mucus penetration and enable efficient intracellular delivery. In a cigarette smoke extract-induced mouse model, A33 treatment significantly inhibited COPD progression and improved pulmonary senescence, validating its therapeutic efficacy. Collectively, these findings introduce a promising local treatment strategy for COPD.

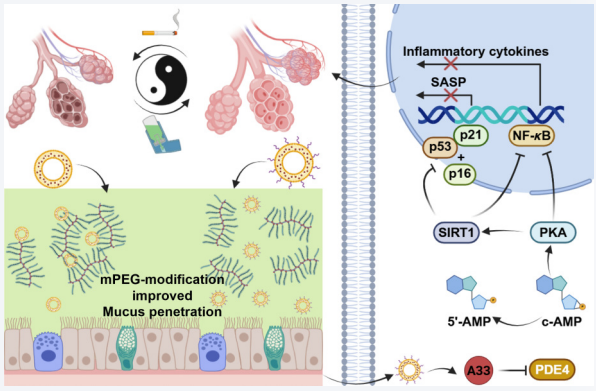

KEYWORDS: chronic obstructive pulmonary disease (COPD), phosphodiesterase 4B (PDE4B) inhibitor, anti-inflammatory, senescence, senescence-associated secretory phenotype (SASP)

1 Introduction

Chronic obstructive pulmonary disease (COPD) has become a global epidemic spreading in low- and middle-income countries, with a characterization of poorly reversible airflow obstruction accompanied by persistent airway inflammation [1]. The clinical therapeutic strategies combining bronchodilators with corticosteroids can only alleviate symptoms of airflow obstruction but are unable to delay pulmonary tissue damage and functional decline [2]. Inflammation is the hallmark of COPD, caused mainly by the inhalation of pollutants such as cigarette smoke or recurrent respiratory infections [3]. The chronic inflammatory environment can induce cellular senescence and impair the epithelial cells' repair function, as well as immune cell-based senescent cell clearance [4, 5]. Moreover, the remaining senescent cells secreted a characteristic profile of inflammatory proteins known as the

Received: November 13, 2025; **Revised:** January 23, 2026
Accepted: January 28, 2026

✉Address correspondence to Xueming Li, xuemingli@njtech.edu.cn; Qiyue Wang, qiyue.wang@njtech.edu.cn

senescence-associated secretory phenotype (SASP), which could accelerate COPD progression and cause nearby normal cells to senesce via the paracrine secretion of inflammatory cytokines [6]. Therefore, effectively regulating the pulmonary inflammatory environment and reducing the release of inflammatory cytokines could be an attractive therapeutic strategy for COPD, which urgently requires development.

Phosphodiesterases (PDEs) are considered the intracellular enzymes that catalyze the hydrolysis of cyclic guanosine monophosphate (cGMP) and cyclic adenosine monophosphate (cAMP), functioning as second messengers and regulators of a wide array of physiological processes. PDE4, which controls cAMP degradation in epithelial cells, smooth muscle cells, and immune cells, has been considered an attractive therapeutic target in the treatment of COPD by regulating nuclear factor kappa-light-chain-enhancer of activated B cells (NF-κB)-based inflammatory responses [7]. Even though Roflumilast, a PDE4 inhibitor, has been approved by the U. S. Food and Drug Administration (FDA) for clinical application, the pan-PDE4 inhibitors exhibit serious intolerable side effects, such as emesis, headache, and diarrhea, due to their poor selectivity on the phosphodiesterase 4 (PDE4) subfamily, especially for the unselective inhibition of PDE4D [8]. Several investigations have confirmed that PDE4B, but not PDE4D, is the key regulator in inflammatory generation, which has promoted the development of PDE4B-selective inhibitors with tolerable anti-inflammatory effects [9, 10]. In this study, we evaluated a novel PDE4B-selective inhibitor, A33, for its anti-inflammatory effects in the lungs of patients with COPD and its potential to counteract pulmonary senescence. A33 (CAS No. 915082-52-9) is a potent and highly selective PDE4 inhibitor (PDE4B IC_{50} of 15 nM; PDE4D IC_{50} of 1.7 μM) with moderate solubility in dimethyl sulfoxide (DMSO) (25 mg/mL) and poor aqueous solubility, showing a C_{max} of 8.7 μg/mL and an area under curve (AUC) of 52.3 μg·h/mL in mice after oral administration (2 mg/kg) [11]. However, the systematic delivery of PDE4B inhibitors exhibits dose-dependent side effects, which severely limit their clinical application prospects [12]. Therefore, considerable effort is needed to achieve effective pulmonary accumulation of PDE4B inhibitors.

The pulmonary local delivery system has been considered the most effective drug delivery route for local disease treatment and is regarded as a promising direction for pharmaceutical research [13]. However, the lungs of COPD patients with inflammation-induced structural remodeling generate a thick and sticky mucus layer, which acts as a physical barrier, preventing the effective delivery of drugs to targeted epithelial cells [14–16]. The glycoproteins secreted by goblet cells crosslink to form a gel network structure, capturing inhaled foreign matter and toxins [17]. The investigation suggested that only the drug delivery system that meets the requirements in particle size, surface charge, and surface hydrophilicity could rapidly cross this mucus barrier and achieve effective drug delivery. Several delivery systems have been designed to avoid mucus traps [18–21]. Using PEG decoration in a drug delivery system can form a hydration layer on the particle surface, which reduces bonding to glycoproteins and achieves rapid mucus penetration [22–24].

Herein, we developed a mucus-penetrating liposome drug delivery system for the pulmonary delivery of a PDE4B inhibitor, targeting the progression of chronic inflammation and tissue senescence in COPD lungs. The anti-inflammatory efficiency of A33 was evaluated in both epithelial cells and alveolar macrophages by measuring the expression of pro-inflammatory proteins. The potential of A33 in regulating epithelial cell senescence was evaluated by analyzing the secretion of SASP. To achieve effective pulmonary delivery of A33, we prepared A33-loaded mucus-penetration liposomes and optimized the amount of mPEG-DSPE incorporated into the liposome formulation. The mucus penetration ability of liposomes was confirmed both *in vitro* and *in vivo*. The intracellular effectively reduces the expression of inflammatory proteins and the secretion of SASP in senescent cells in the cigarette smoke-induced COPD mouse model. This work highlights the design of an effective respiratory mucus-penetrated liposome to improve COPD through PDE4B-mediated anti-inflammatory effects.

2 Experimental

2.1 Materials and cell lines

Soy lecithin was purchased from Xi'an Jinxiang Pharmaceutic Adjuvant Ltd. (Xi'an, China). Cholesterol and mucin from the porcine stomach (Type II) were purchased from Sigma-Aldrich (Shanghai, China). DSPE-$mPEG_{2k}$ (1,2-distearoyl-sn-glycero-3-phosphoethanolamine-N-[methoxy(polyethylene glycol)-2000]) was obtained from Xi'an Ruixi Biological Technology Co., Led. (Xi'an, China). A33 was purchased from Tocris Bioscience (Shanghai, China). 3-(4,5-dimethylthiazol-2-yl)-2,5-diphenyltetrazolium bromide (MTT), 4',6-diamidino-2-phenylindole (DAPI) staining solution, lipopolysaccharide (LPS), and 1,1'-dioctadecyl-3,3,3',3'-tetramethylindotricarbocyanine iodide (DIR) dye were obtained from Jiangsu KeyGEN BioTECH Co., Ltd. (Nanjing, China). The cAMP ELISA kit was purchased from COIBO BIO Biotechnology Co., Ltd. (Shanghai, China). The RNAeasy™ RNA isolation kit, BeyoRT™ II cDNA synthesis kit, BeyoFast™ SYBR Green qPCR Mix, SA-β-gal staining kit, reactive oxygen species (ROS) assay kit, and DNA damage assay kit were purchased from Beyotime Biotechnology (Shanghai, China). Real-time quantitative polymerase chain reaction (qPCR) primers were obtained from Shanghai Biochip Co., Ltd. (Shanghai, China). All the primary antibodies were purchased from Affinity Biosciences (Cincinnati, USA). All other chemical reagents were purchased from Sinopharm Chemical Reagent Co., Ltd. (Shanghai, China).

BEAS-2B cells and iBMDM cells were purchased from Jiangsu KeyGEN BioTECH Co., Ltd. (Nanjing, China). BEAS-2B cells were cultured in DMEM/F12 medium containing 10% fetal bovine serum (FBS) and 1% Penicillin/Streptomycin. The iBMDM cells were cultured in DMEM medium supplemented with 10% FBS and 1% Penicillin/Streptomycin. All cells were cultured in a humidified incubator at 37 °C, supplemented with 5% CO_2, for further use.

2.2 Formulation preparation and characterization

Soy lecithin and cholesterol were mixed at different weight ratios (3:1, 6:1, or 9:1) in methanol, and A33 was then mixed with lipid materials at various weight ratios (1:4, 1:8, or 1:10). The organic solvent in the mixture was evaporated using a rotary evaporator to form a thin film, followed by a vacuum to remove the solvent residue. For film hydration, suitable PBS was added to the dry lipid film, followed by vortexing to suspend the lipid materials in the solution at the total lipid concentration of 2 mg/mL. The suspension was sonicated in a water bath for 5 to 15 min at various temperatures (35, 40, or 45 °C), followed by extrusion 3 to 10 times,

and then passing through polycarbonate membranes with a pore size of 200 nm to obtain the A33-loaded normal liposome (A33@Lips). The mPEG-modified A33 liposome (A33@mPEG-Lips) was prepared using a similar process. Different amounts of DSPE-mPEG2k (1%, 5%, and 10%) were mixed with lipid materials to prepare the dry film, followed by a hydration process under the same conditions.

The A33 content in A33@Lips and A33@mPEG-Lips was analyzed using the high-performance liquid chromatography with ultraviolet detection (HPLC-UV) assay with the following conditions: the mobile phase of water:acetonitrile = 20:80, detection wavelength of 220 nm, column temperature of 35 °C, and flow rate of 1.0 mL/min. The A33 encapsulation efficiency was calculated by equations (Eqs. (1) and (2)):

$$\text{Drug loading}\,(\%) = \frac{m_{\text{A33}} - m_{\text{uA33}}}{m_{\text{A33}} - m_{\text{uA33}} + m_{\text{Lipid}}} \times 100\% \quad (1)$$

$$\text{Encapsulation efficiency}\,(\%) = \frac{m_{\text{A33}} - m_{\text{uA33}}}{m_{\text{A33}}} \times 100\% \quad (2)$$

where m_{A33} is the weight of A33 added in the formulation, m_{uA33} is the weight of the unloaded A33, and m_{Lipid} is the total weight of Lipid materials in the formulation preparation.

The suitable amounts of fresh-prepared A33@Lips and A33@mPEG-Lips were diluted in an aqueous solution to similar concentrations. The hydrodynamic diameter and zeta potential of the formulations were measured using a Zeta Potential and Particle Size Analyzer (90Plus Zeta, Brookhaven Instruments Corporation, USA). Their morphology is analyzed by transmission electron microscopy (TEM, HT7700, Hitachi, Japan). The stability of the A33@Lips and A33@mPEG-Lips was evaluated by measuring their particle size, polydispersity index (PDI), and zeta potential difference. The suitable amounts of formulations were stored at 4 °C for 48 h, and their particle size and zeta potential were measured at different time intervals.

The surface mucin adsorption ability of formulations was determined. Porcine stomach mucin (Type II) and sodium alginate were dissolved in water overnight to prepare a stock solution. To prepare artificial airway mucus, the mucin solution, sodium salt solution of d-(+)-gluconic acid δ-lactone (GDL) solution, and sodium alginate solution were mixed and diluted to a final concentration (mucin of 43.75 mg/mL, GDL of 49.84 mg/mL, sodium alginate of 21 mg/mL). Formulations with suitable concentrations were incubated with the artificial mucin solution for 6 h at 37 °C (volume ratio of 1:1). The liposomes were then collected via ultra-high-speed centrifugation, and the adsorbed mucin protein was analyzed using the sodium dodecyl sulfate polyacrylamide gel electrophoresis (SDS-PAGE) assay and quantified using the bicinchoninic acid (BCA) kit.

To evaluate the *in vitro* release of A33, fresh-prepared A33@Lips and A33@mPEG-Lips were transferred into dialysis bags with a 3500 Da cut-off molecular weight, followed by incubation in PBS buffer at pH 7.4 and 5.4, respectively. At regular time intervals, 1 mL of release medium was collected, and an equal volume of fresh medium was replenished. The concentration of A33 in the culture medium was analyzed by the HPLC assay described above, and the cumulative release of A33 was calculated.

The dispersion performance of A33@mPEG-Lips was evaluated using the next generation impactor (NGI, Copley Scientific Ltd., Nottingham, UK), as described previously [25]. Briefly, the NGI was assembled with an induction port and an artificial throat, followed by adjustment of the airflow rate using a vacuum pump (HCP5, Copley Scientific Ltd., Nottingham, UK) and an airflow meter (TPK 2000, Copley Scientific Ltd., Nottingham, UK). A33@Lips and A33@mPEG-Lips solutions were loaded into the vibrating mesh nebulizer, which was connected to a mouthpiece adapter. The formulation was subsequently aerosolized for 3 min, and the aerosols were inhaled into the NGI at an airflow rate of 30 L/min with a conductance time of 3 s at room temperature. The deposition of formulations in each stage was dispersed in PBS, and the A33 concentration was analyzed using the HPLC assay under the above conditions, followed by the calculation of the mass median aerodynamic diameter (MMAD) and geometric standard deviation (GSD).

2.3 MTT assay, real-time PCR assay, and Western blot assay

For the MTT assay, the MTT solution was added to the wells at a final concentration of 0.5 mg/mL, followed by incubation at 37 °C in the dark for 3 h. The incubation medium in each well was removed and washed three times with cold PBS, followed by the addition of 100 μL of DMSO. The plates were placed on the microplate reader, and the absorbance was measured at 570 nm.

For real-time PCR analysis, treated cell samples were washed and lysed, followed by extraction of total RNA using the RNAeasy™ RNA isolation kit. The concentration and purity of extracted total RNA were measured using the microplate reader at 260 and 280 nm. The BeyoRT™ II cDNA synthesis kit was used to convert total RNA to cDNA, following the manufacturer's instructions. The SYBR Green qPCR Mix was used to run RT-PCR on a LightCycler 480 Instrument (Roche, USA) using target primers (Table S1 in the Electronic Supplementary Material (ESM)).

For the Western blot assay, total protein was isolated from the cell sample lysates by incubating cells with radio immunoprecipitation assay (RIPA) lysis buffer, followed by centrifugation at 10,000*g* for 10 min. Protein concentration was determined using the BCA kit. Equal amounts of protein samples were loaded and separated in the PROTEAN polyacrylamide gel, followed by transferring to polyvinylidene fluoride (PVDF) membranes. Membranes were then blocked with a blocking buffer for 2 h, followed by incubation with primary antibodies overnight. The membranes were then washed with the staining buffer and incubated with fluorescent-coupled secondary antibodies. The images of the target bands were recorded using a FUJIFILM LAS-4000 luminescent image analyzer (FUJIFILM Medical Systems Inc., USA).

2.4 Cytotoxicity evaluation

BEAS-2B cells and iBMDM cells were seeded in 96-well plates at a concentration of 1×10^4 cells per well, respectively, for overnight attachment in an incubator under 5% CO_2 at 37 °C in a 95% humidified atmosphere. To evaluate the cytotoxicity of A33, A33@Lips, and A33@mPEG-Lips, a series of solutions with various A33 concentrations were co-incubated with cells for 48 h, and cell viability was measured using the MTT assay. The cytotoxicity of cigarette smoke extracts (CSE) on epithelial cells was also determined. The CSE was prepared in accordance with the previous description [26]. BEAS-2B cells were co-incubated with CSE at different concentrations for 48 h, and cell viability was evaluated using the MTT assay described above.

To evaluate the effects of A33 on CSE-induced inflammation, we measured the viability of BEAS-2B cells when co-incubated with both A33 and CSE in different culturing orders. To evaluate the potential of A33 in treating CSE-induced inflammation, cells were first incubated with CSE (2.5%) for 24 h and then replaced with various concentrations of A33, followed by continued culturing for 48 h. To evaluate the potential of A33 to prevent CSE-induced inflammation, cells were first incubated with various concentrations of A33 for 24 h, and then CSE (2.5%) was added, followed by continued culturing for an additional 24 h. The cell viability was analyzed using the MTT assay described above.

2.5 Anti-inflammatory evaluation

To evaluate the anti-inflammation ability of A33, A33@Lips, and A33@mPEG-Lips, BEAS-2B cells and iBMDM cells were first incubated with CSE (2.5%) for 24 h. Then, the culture medium was replaced with a fresh culture medium containing 50 nM of A33, and their formulations and cells were cultured for 48 h. The expression of pro-inflammatory proteins, including NF-κB, IL-6, IL-1β, and tumor necrosis factor-α (TNF-α), was evaluated by measuring mRNA levels using the qPCR assay. The expression of key regulator proteins was analyzed using the Western blot assay. The cAMP level in treated cells was also measured using the enzyme-linked immunosorbent assay (ELISA) kits following the manufacturer's instructions. The levels of secreted pro-inflammatory cytokines in the culture medium were further determined using ELISA kits.

2.6 Anti-senescence evaluation

2.6.1 Senescence cell model

The senescence epithelial cell model was stimulated using the hydrogen peroxide assay. Briefly, BEAS-2B or iBMDM cells were seeded into 6-well plates (2×10^5 cells/well) and cultured for 24 h until the cell density reached 80%. Cells were stimulated with doxorubicin (100 nM) for 24 h, followed by twice PBS washes. Then, cells were kept in culture with fresh medium for 4 days.

2.6.2 Senescence biomarker regulated by A33

To evaluate the anti-senescence ability, senescent cells were incubated with A33 and its formulations (50 nM) for 48 h. The expression of senescence-associated β-galactosidase (SA-β-gal) was evaluated using the SA-β-gal staining kit. In brief, cells were fixed at room temperature for 15 min, followed by the addition of the staining mixture and incubation overnight at 37 °C. After that, the cells were washed with PBS, and the SA-β-gal-positive cells were observed using a microscope. The mRNA levels of SASP markers (TGF-β1, TNF-α, matrix metalloproteinases-12 (MMP-12), IL-1β, and IL-6) and senescent-related regulator (SIRT1) were determined using the qPCR assay. The expression of $p16^{INK4a}$, p21, SIRT1, and FoxO3 proteins was detected and visualized using a western blot assay. The SASP release was evaluated by the ELISA assay.

2.6.3 DNA damage assay

Senescent BEAS-2B cells were incubated with A33 (50 nM) for 48 h. Then, the cells were washed, fixed, and stained with γ-H2AX primary antibody, followed by incubation with secondary IR dye-conjugated antibodies (1:10,000, LI-COR). After the DAPI was stained, the fluorescence signals of γ-H2AX were observed using a confocal laser scanning microscope, and the fluorescence intensity was calculated using ImageJ software.

2.6.4 ROS generation assay

Senescent BEAS-2B cells were co-incubated with fresh FBS-free culture medium containing A33 (50 nM) for 48 h at 37 °C. For the ROS generation assay, 1 mL of 2',7'-dichlorodihydrofluorescein diacetate (DCFH-DA) solution (10 μM) was added to cells and co-incubated at 37 °C for 30 min in the dark. After washing the cells with PBS 3 times, the ROS levels in BEAS-2B cells from different groups were observed using a fluorescence microscope. The fluorescence intensity was calculated using the ImageJ software.

2.7 Mucus penetration assay

The multiple particle tracking assay was also applied to evaluate the trajectory of particles in the mucus sample. A33@PLGA-NPs was prepared using the double emulation assay described before [27]. The A33@PLGA-NPs, A33@Lips, and A33@mPEG-Lips were mixed with artificial mucus. After equilibration for 30 min at room temperature, 20-s videos of particle movement and their trajectories were captured using the NanoSight (NS300, Malvern Panalytical, UK). The particle movement was converted into metric displacement in both the X and Y directions, and the mean square displacement (MSD) was calculated by equation (Eq. (3)):

$$\mathrm{MSD} = (X_{\Delta t})^2 + (Y_{\Delta t})^2 \quad (3)$$

The interaction of liposomes and mucin was analyzed using a rotational rheometer (HDR-2, TA, USA). The viscosity of artificial mucus after being mixed with A33@Lips and A33@mPEG-Lips was measured at the shear rate $1–10^3$ s^{-1} to cover mucus shear static during static breathing (0.5 s^{-1}) and dynamic coughing ($10^3–10^4$ s^{-1}). The storage modulus (G') and loss modulus (G'') of various samples were determined by oscillatory frequency sweep measurements at a 0.5% strain amplitude with a frequency range of 0.05–1.6 Hz, encompassing the normal breathing rate (0.5 Hz) [23].

The Transwell assay was used to evaluate the effect of mPEG modification on improving mucus permeation. The Transwell insert with a pore size of 0.4 μm was placed on a 6-well plate and covered with 300 μL of artificial mucus, as described [28]. The DIR-encapsulated liposomes (DIR@Lips and DIR@mPEG-Lips) were added into the upper chambers, and the bottom chamber was filled with 1 mL of PBS. The plates were incubated in a shaker (100 rpm) at 37 °C in the dark. At different time intervals, 100 μL of sample from the bottom chamber was collected, and the same amount of fresh buffer was supplemented. The fluorescence in the samples was quantified using a fluorescence detector (F-2710, Hitachi, Japan).

2.8 Cellular uptake assay

BEAS-2B cells and iBMDM cells were seeded into 6-well plates at a density of 2×10^5/well, respectively, and allowed to attach overnight. Then, the culture medium was replaced with an FBS-free medium containing free DIR, DIR@mPEG-Lips, and mucin pre-incubated DIR@mPEG-Lips, respectively, with an equivalent DIR concentration of 10 μg/mL. Cells in all groups were incubated at 37 °C for 4 h in the dark. The cellular uptake was analyzed by flow cytometry using a BD LSRII flow cytometer (BD Biosciences, CA, USA). For microscopy observation, cells were washed, fixed, and stained with DAPI. The cellular uptake of different groups was observed under an IX73 fluorescence inverted microscope (Olympus, Tokyo, Japan) 4 h after incubation. The fluorescence intensity was calculated using ImageJ software.

2.9 Macrophage polarization

iBMDM cells were seeded into 6-well plates at a density of 2×10^5/well and allowed to attach overnight. Cells were incubated with CSE (2.5%) for 24 h and then treated with A33@Lips and A33@mPEG-Lips for an additional 48 h. The iBMDM polarization was then evaluated by staining with fluorescein isothiocyanate (FITC)-anti-CD11b, allophycocyanin (APC)-anti-iNOS, and phycoerythrin (PE)-anti-CD206 and analyzed using flow cytometry.

2.10 COPD mouse model

BALB/c mice at 8–10 weeks of age were purchased from Jiangsu Qinglongshang Biotechnology Co., Ltd. All animal experiments were approved by the Animal Care and Use Committee of Nanjing Tech University (No. 20230304-04). To establish the COPD mouse model, the BALB/c mice were exposed to the smoke generated from 1R6F Research Cigarettes (University of Kentucky, USA) as described previously [29]. Briefly, mice were exposed to cigarette smoke (500 mg/m^3 total particulate matter) in a whole-body exposure system (Beijing Huironghe Technology Co., Ltd., China) for 60 min, twice a day, 5 days a week, for a total of 12 weeks. The mice were also administered LPS (0.1 mg/kg) every 6 weeks by the intratracheal route for a total of two times. Cigarette smoke-induced pulmonary structural remodeling and immune cell infiltration in mouse lungs were observed by H&E (hematoxylin and eosin) staining and immunofluorescence assays to stain CD11b, iNOS, and CD206.

2.11 Biodistribution

To investigate the biodistribution of the formulation, the COPD model mice were randomly divided into 3 groups and administered free DIR, DIR-labeled Lips, and DIR-labeled mPEG-Lips (equivalent DIR dose of 1 mg/kg) via intratracheal insufflation [30]. The fluorescence images of the mice were obtained at 1, 2, 4, 6, and 24 h after administration using *in vivo* imaging system (IVIS) imaging. After the last time interval, mice were euthanized, and their major organs were collected and imaged. The A33 retention in the lungs was also investigated by measuring A33 concentration in lung tissue homogenate using the same HPLC conditions.

2.12 Anti-inflammatory effects of A33 *in vivo*

COPD model mice were randomly divided into 4 groups (n = 5) and treated with PBS, A33 alone, A33@Lips, and A33@mPEG-Lips at a dose equivalent to 2.5 mg/kg A33 by intratracheal insufflation every three days for 5 times. After the treatment course, mice were euthanized, followed by a dissection of the lung and other major organs. The half lungs were fixed, embedded, and further stained with H&E to confirm the pulmonary structure. The lung dry/wet ratio was also determined by measuring the weight of the original and dried lung tissue. The expression of inflammatory proteins, SASP markers, and the anti-inflammatory regulator SIRT1 was determined in lung tissue homogenate using qPCR and western blot assays. The pro-inflammatory protein secreted was measured in bronchoalveolar lavage fluid (BALF) using the ELISA kit. The immune cell infiltration and essential senescence-maker proteins were observed using immunofluorescence and immunohistochemical assays to evaluate the anti-inflammatory and senescence effects against the ability of A33.

2.13 Safety investigation

The BEAS-2B cells and iBMDM cells were cultured in 96-well plates at a density of 1×10^4 cells per well, and A33@mPEG-Lips were added and incubated with the cells at various concentrations for 48 h. The cytotoxicity of the formulation was calculated by measuring cell viability using the MTT assay. The liver toxicity of A33@mPEG-Lips was evaluated by measuring the serum levels of alanine aminotransferase (ALT) and aspartate aminotransferase (AST). The cytotoxicity of A33@mPEG-Lips was also measured via H&E staining of major organs from healthy mice.

2.14 Statistical analysis

The software used for data analysis was SPSS 22.0 (IBM Corp., Armonk, NY, USA), and the data were statistically analyzed using one-way analysis of variance (ANOVA). The results are expressed as the mean ± standard deviation (SD), and $P < 0.05$ was considered statistically significant.

3 Results

3.1 PDE4B inhibitor against CSE-induced inflammation

A33, as a selective PDE4B inhibitor, was expected to be potent in inhibiting cellular inflammation induced by CSE. We first measured the cytotoxicity of A33 on both bronchial epithelial cells and macrophages. There was no significant cytotoxicity observed in either BEAS-2B cells or iBMDM cells, even when the A33 concentration reached 5 μM (Figs. 1(a) and 1(b)), suggesting that A33 has low toxicity in normal respiratory cell types. To determine the concentration of CSE solution in inducing cellular inflammation, we also evaluated the toxicity of CSE in BEAS-2B cells and iBMDM cells. A significant cell toxicity was observed after co-incubation with the CSE solution at concentrations higher than 2.5%, indicating that CSE-based oxidative stress could potentially reduce cell proliferation and induce epithelial damage (Figs. 1(c) and 1(d)). Thus, we selected a CSE concentration of 2.5% for further cellular incubation and evaluated the protection or prevention of A33 on BEAS-2B cells. To determine the ability to relieve inflammation-induced cell death, BEAS-2B cells were first incubated with CSE, followed by replacement with an A33-containing medium. The data suggested that A33 exhibited epithelial cell protection with increased cell viability after CSE-induced cell damage (Fig. 1(e)). Moreover, the ability of A33 to prevent inflammation-induced cell death was further evaluated by switching the co-incubation sequence of CSE and A33. Similar to the effective protection of inflammatory-damaged cells, A33 at high concentrations improved cell viability against CSE-based cell death and exhibited potential for inflammatory prevention (Fig. 1(f)).

To confirm the anti-inflammatory effects of A33, we further determined the expression of key pro-inflammatory proteins and cytokines at both mRNA and protein levels. As a selective PDE4B inhibitor, the regulation of A33 on intracellular second messenger cAMP was measured using an ELISA kit. As shown in Fig. 1(g), A33 incubation can increase cAMP levels in both BEAS-2B cells and iBMDM cells, confirming its ability to inhibit PDE4 function and promote intracellular cAMP accumulation. For the CSE-induced cell, A33 treatment also significantly recovered cAMP levels. Moreover, we found that CSE incubation elevated the mRNA levels of NF-κB and IL-6 in BEAS-2B cells, and A33 treatment reduced the expression of these pro-inflammatory

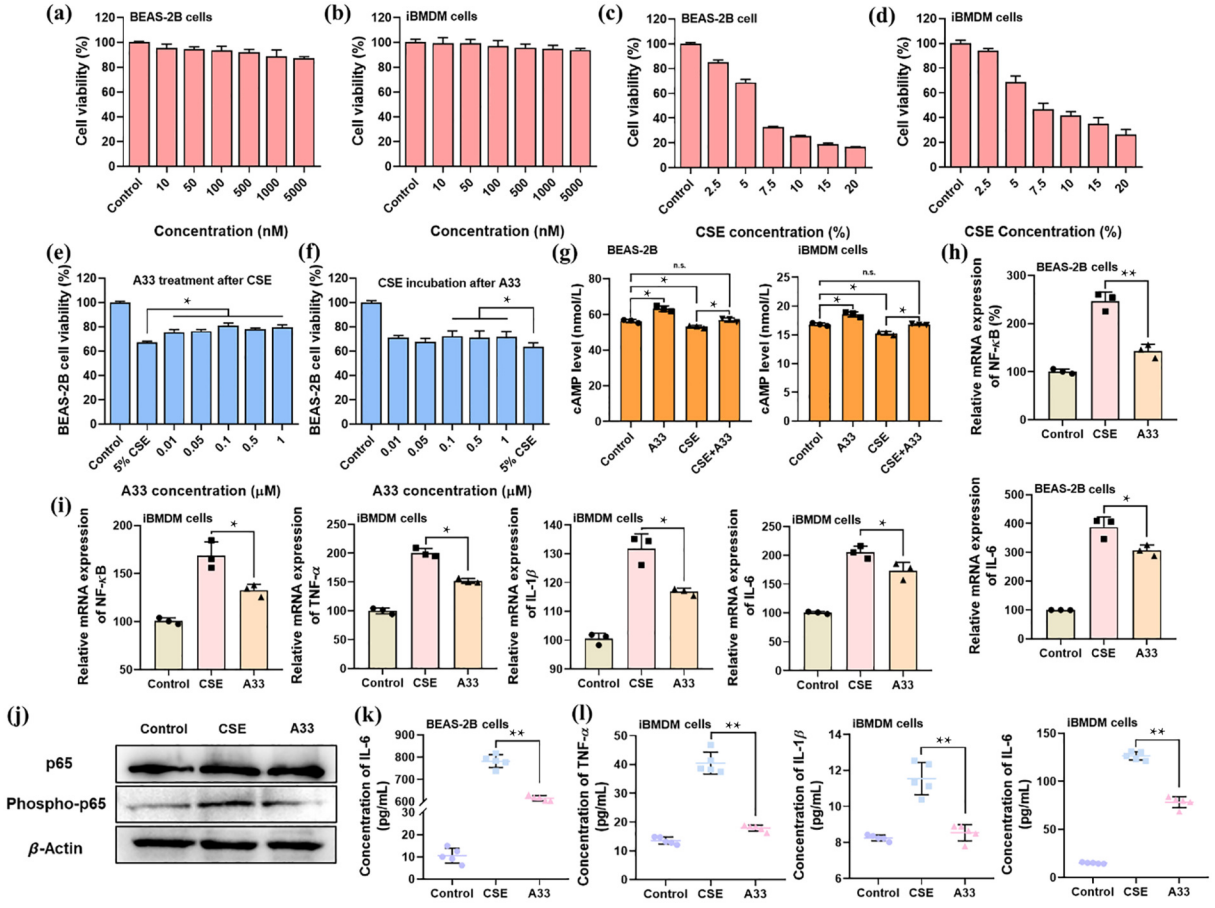

Figure 1 A33 regulates the CSE-induced inflammatory environment. Cytotoxicity of A33 on (a) BEAS-2B and (b) iBMDM cells (n = 6). Cytotoxicity of CSE solution in (c) BEAS-2B and (d) iBMDM cells (n = 6). (e) Effects of A33 in treating CSE-induced cell death (n = 6). (f) Effects of A33 in preventing CSE-induced cell death (n = 6). (g) The difference in intracellular cAMP in mRNA levels from BEAS-2B and iBMDM cells before and after incubation with CSE and A33, respectively (n = 3). (h) The inhibition of intracellular NF-κB and IL-6 in mRNA levels from CSE-induced BEAS-2B cells after A33 treatment. (i) The inhibition of intracellular NF-κB, TNF-α, IL-1β, and IL-6 in mRNA levels from CSE-induced iBMDM cells after A33 treatment. (j) Western blot bands of protein expression in p65 and phospho-p65 from BEAS-2B cells. The inhibition of secreted pro-inflammatory cytokines in (k) BEAS-2B cells and (l) iBMDM cells after A33 treatment, respectively. $^*P < 0.05$, $^{**}P < 0.01$.

regulators (Fig. 1(h)). A similar result was also observed on iBMDM cells. CSE induction increased the expression of NF-κB and downstream pro-inflammatory cytokines, such as TNF-α, IL-1β, and IL-6, at the mRNA level, while A33 treatment significantly inhibited the activation of the NF-κB-based inflammatory pathway (Fig. 1(i)). Similar data were observed on the protein levels. The expression of p65 and phospho-p65 in BSAE-2B cells was measured using a western blot assay with β-actin as an internal reference. After incubation with A33, the phosphate p65 was increased after CSE inducement and decreased after A33 treatment, again suggesting the potential of A33 in regulating the inflammation signaling pathway (Fig. 1(j) and Fig. S1 in the ESM). In addition, the secretion of pro-inflammatory cytokines from BEAS-2B cells (IL-6) and iBMDM cells (TNF-α, IL-1β, and IL-6) was also significantly decreased after A33 incubation compared to the CSE-induced model group (Figs. 1(k) and 1(l)), further confirming that A33 exhibits potential to inhibit inflammation in the respiratory epithelium.

3.2 PDE4B inhibitor regulates cellular senescence

Cellular senescence has been reported as a key factor in maintaining a chronic inflammatory microenvironment. The continuous accumulation of intracellular inflammation may also accelerate organ senescence. Based on the anti-inflammatory ability of A33 in reducing NF-κB pathway activation, we hypothesized that it may have a similar potential in combating cellular senescence. BEAS-2B cell senescence was induced by incubation with doxorubicin, and the mRNA level of transforming growth factor beta 1 (TGFB1), p16, and IL6 was monitored using the qPCR assay to confirm the cellular senescence. After doxorubicin induction, TGFB1 expression, an early senescence marker, increased rapidly within one day and then slowly decreased, while p16 and IL-6, late markers of senescence, exhibited a significant elevation starting from day three and continued to increase (Fig. 2(a)). Moreover, the ratio of SA-β-gal-positive cells was also significantly increased compared to the control, indicating that the senescent BEAS-2B cells were successfully induced (Figs. 2(b) and 2(c)).

The effect of A33 treatment on the expression of SASP in senescent cells was then evaluated at both mRNA and protein levels. After incubation with A33, senescent BEAS-2B cells exhibited an elevation of SIRT1 but a decline in representative SASP markers (TNF-α, MMP-12, IL-1β, and IL-6) at the mRNA level (Fig. 2(d)). Consistent with the q-PCR data, the secretion of senescence-related cytokines was also significantly decreased in A33-treated cells compared to untreated senescent cells, suggesting that the PDE4B inhibitor has the potential to alleviate the cellular aging

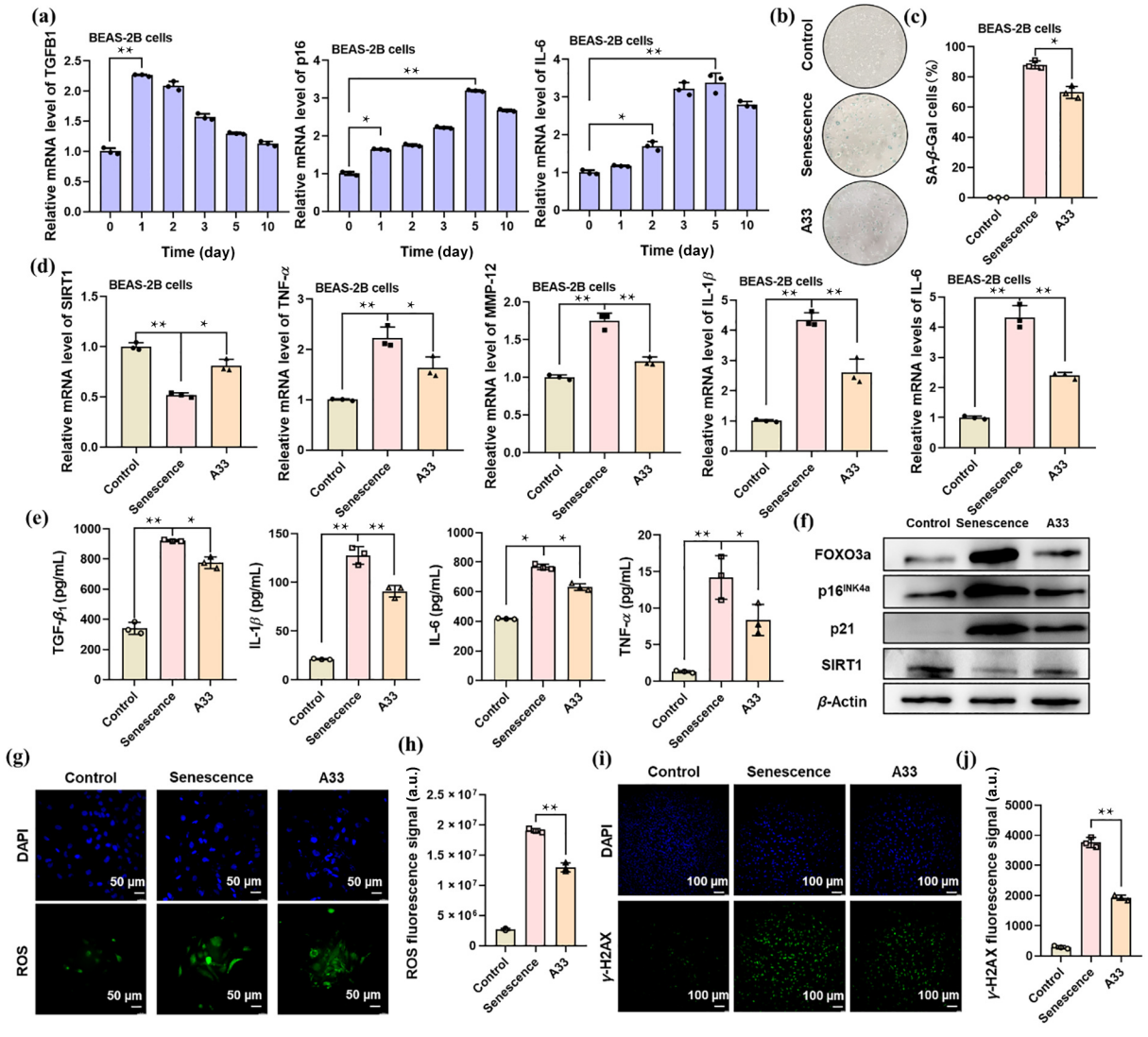

Figure 2 Effects of A33 in inhibiting the cellular senescence of respiratory epithelial cells. (a) The expression of TGFB1, p16, and IL-6 in mRNA levels in senescent BEAS-2B cells induced by doxorubicin. (b) The representative images of senescent BEAS-2B cells stained by the SA-β-Gal kit and (c) the quantitative analysis of the SA-β-Gal-positive cell ratio. (d) The difference in intracellular SIRT1, TNF-α, MMP-12, IL-1β, and IL-6 at mRNA levels from senescent BEAS-2B cells after incubation with A33. (e) The difference in secreted TGF-β1, TNG-α, IL-1β, and IL-6 cytokines from senescent BEAS-2B cells after incubation with A33. (f) The western blot bands of protein expression for FOXO3a, $p16^{INK4a}$, p21, and SIRT1 in senescent BEAS-2B cells. (g) The representative images and (h) quantitative analysis of ROS fluorescence signal intensity from senescent BEAS-2B cells stained by the ROS assay kit after incubating with A33. (i) The representative images and (j) quantitative analysis of γ-H2AX fluorescence signal intensity from senescent BEAS-2B cells stained by the DNA damage assay kit after incubating with A33. $^*P < 0.05$, $^{**}P < 0.01$.

process (Fig. 2(e)). Additionally, the activation of senescence-related signaling pathways was further investigated using a Western blot assay. The intracellular protein expression of FoxO3a, $p16^{INK4a}$, and p21 was reduced, but SIRT1 was recovered compared to the untreated group, indicating that A33 could reduce oxidative stress-based cellular injury through the AMPK/SIRT1/FOXO pathway and against inflammatory-induced senescence via p21- or p16-based cyclin-dependent kinases regulation (Fig. 2(f) and Fig. S2 in the ESM).

Intracellular oxidation imbalance occurs during cell senescence [31]. By inhibiting PDE4B activation, A33 significantly increased SIRT1 expression and enhanced cellular antioxidative ability. The ROS fluorescence signals in senescent BEAS-2B cells decreased after A33 treatment, and the calculated mean fluorescence intensity (MFI) showed that A33 reduced the ROS level by approximately 40% compared to the senescent groups, confirming its ability to eliminate ROS in senescent cells (Figs. 2(g) and 2(h)). Moreover, we also evaluated the DNA damage induced by the generated ROS using the γ-H2AX assay. The senescent BEAS-2B cells exhibited an apparent green fluorescence signal compared to the control groups, which was significantly reduced after treatment with A33, suggesting that A33-mediated SIRT1 restoration enhanced cellular antioxidant ability and repaired intracellular DNA damage (Figs. 2(i) and 2(j)).

3.3 Formulation characterization

To achieve effective A33 pulmonary delivery, we designed an A33-loaded liposome with mPEG modification with the expectation of improving respiratory mucus penetration. The liposome formulation was first optimized by the single-factor prescription evaluation. With the liposome particle size and A33 encapsulation as key parameters, the data suggested that a lecithin/cholesterol

weight ratio of 6:1 and an A33/Lipid weight ratio of 1:10 were suitable prescriptions for the preparation of A33-loaded liposomes (A33 encapsulation rate around 90% with the lower particle size) (Fig. S3 in the ESM). Moreover, the preparation parameters were selected as follows: a sonication time of 15 min, a sonication temperature of 40 °C, and 5 extrusion processes (Fig. S4 in the ESM). Then, A33-loaded liposomes were prepared using the optimized parameters, and they were subsequently characterized. The 1,2-distearoyl-sn-glycero-3-phosphoethanolamine-poly(ethylene glycol) (DSPE-PEG) percentage has little effect on liposome size and A33 encapsulation, and they use 5% mPEG-DSPE (w/w) in liposome preparation and characterization (Fig. S5 in the ESM).

The particle size of blank liposomes was around 171.8 ± 6.2 nm (Fig. 3(a)). After loading A33, the particle size of liposomes was increased to 196.4 ± 3.9 nm. The A33@mPEG-Lips has a sight increased particle size (reaching 221 ± 5.1 nm) compared with A33@Lips, which is due to the hydration layer formed by the mPEG chain on the liposome surface. The A33 loading reached 7.31% ± 0.17% with an encapsulation efficiency of 89.4% ± 1.46%, indicating successful A33 embedment. The zeta potential of A33@mPEG-Lips showed an increase with A33@Lips, indicating that the mPEG might shield the surface charges. The particle size of various formulations was further observed using the TEM assay, which was consistent with the dynamic light scattering (DLS) data. The mPEG modification exhibited no changes in the surface morphology of the A33-loaded liposome (Fig. 3(b)). The stability of blank liposomes, A33@Lips, and A33@mPEG-Lips was investigated by measuring the particle size, PDI, and zeta potential (Figs. 3(c) and 3(d), and Figs. S6 and S7 in the ESM). The data showed that no significant difference was observed in all the formulation groups, suggesting that A33-loaded formulations could maintain their characteristics during the investigation.

To achieve effective pulmonary deposition, the A33-loaded formulation needs to be atomized by the device and inhaled. The stability of formulations' tolerance to shear stress during the atomization process was also evaluated. As shown in Fig. 3(e), the particle size and zeta potential of A33-loaded formulations remain unchanged before and after the atomization process, indicating the potential of the formulation to withstand the shear stress from the inhalation device. The pulmonary deposition of A33-loaded formulations was then evaluated by the NGI assay. After atomization, A33@Lips and A33@mPEG-Lips exhibited similar behavior, mainly depositing at S3 to S5, and no significant difference in MMAD (2.69 vs. 2.71 μm) and GSD (1.90 vs. 1.81) was observed between the two groups, indicating the potential of the A33-loaded formulation for efficacious pulmonary delivery (Fig. 3(f)).

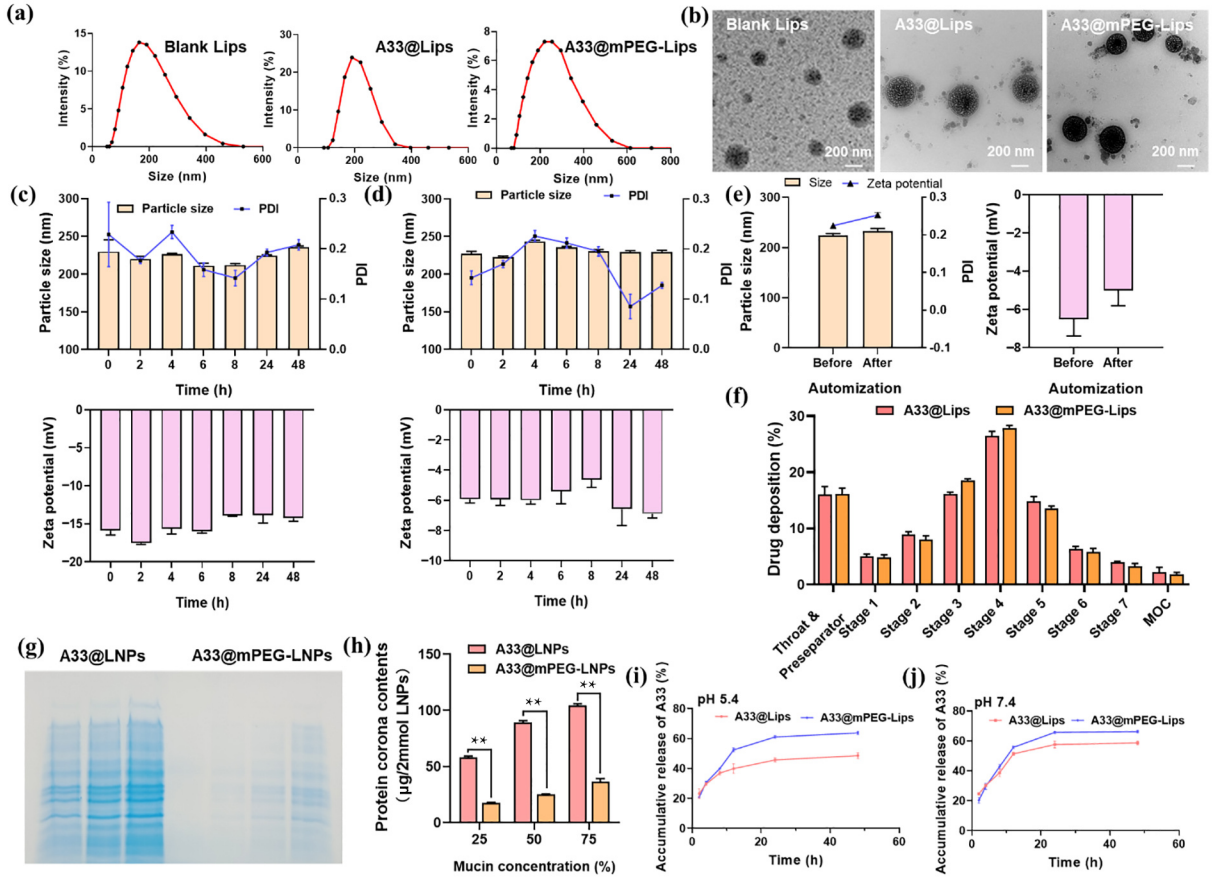

Figure 3 Characterization of A33@mPEG-LNPs. (a) Dynamic light scattering of blank liposomes, A33@Lips, and A33@mPEG-Lips. (b) Morphology of different formulations analyzed by TEM. Stability analysis of (c) A33@Lips and (d) A33@mPEG-Lips by monitoring the particle size and zeta potential, respectively (n = 3). (e) The stability evaluation of A33@mPEG-Lips was assessed by measuring particle size and zeta potential before and after exposure to the tolerance shear stress from the atomizer (n = 3). (f) The NGI deposition analysis of atomized A33@Lips and A33@mPEG-Lips (n = 3). The mucin protein adherent ability on the surface of A33@Lips and A33@mPEG-Lips, respectively, analyzed using (g) SDS-PAGE assay and (h) BCA protein assay kit (n = 3). The A33 release from A33@Lips and A33@mPEG-Lips at (i) pH 5.4 and (j) pH 7.4, respectively (n = 3).

Before reaching the respiratory epithelium, deposited formulations should penetrate the mucus layer and avoid the mucin binding. Therefore, we further determined the mucin absorption of A33@Lips and A33@mPEG-Lips. As shown in Fig. 3(g), the A33@Lips groups exhibited abundant protein absorption compared to the A33@mPEG-Lips determined using the SDS-PAGE assay. Moreover, we quantified surface protein adsorption using the BCA kit, and the data exhibited that mPEG-Lips decreased protein adhesion by around 70% at different mucin concentrations (Fig. 3(h)), indicating that surface PEG modification can form a hydrophilic layer to prevent protein adsorption, which may improve the formulation's mucus penetration.

The drug release was also investigated at both pH 7.4 and pH 5.4 to simulate its release behavior in both extracellular and intralysosomal environments (Figs. 3(i) and 3(j)). A33@mPEG-Lips exhibited a higher cumulative release of A33 compared to the A33@Lips in both pH environments, which is due to the PEG-induced fluidity increment in the interfacial region [32]. Therefore, mPEG-decorated liposomes exhibited better stability, along with an improvement in drug release, making them a potential formulation for the effective pulmonary delivery of A33.

3.4 Mucus penetration analysis *in vitro*

Mucus penetration properties of A33@mPEG-Lips were evaluated using NanoSight to track the trajectories of the nanoparticles in artificial mucus. As shown in Fig. 4(a), the movement of A33@Lips in mucus was impeded compared with that in water, indicating that normal particles could easily be trapped during the pulmonary administration in COPD patients with sticky mucus. While for the A33@mPEG-Lips, the particle movement remained rapid and free compared to the insoluble A33@PLGA-NPs and A33@Lips. Moreover, the geometric average mean square displacement (MSD) values were calculated to quantify the movement behavior of particles. The MSD of A33@Lips significantly reduced in mucus compared to that in water (Fig. 4(b)). While the MSD value of A33@mPEG-Lips is significantly higher than that of A33@PLGA-NPs and A33@Lips under the same conditions. The movement analysis suggested that the particle surface may affect its mucus

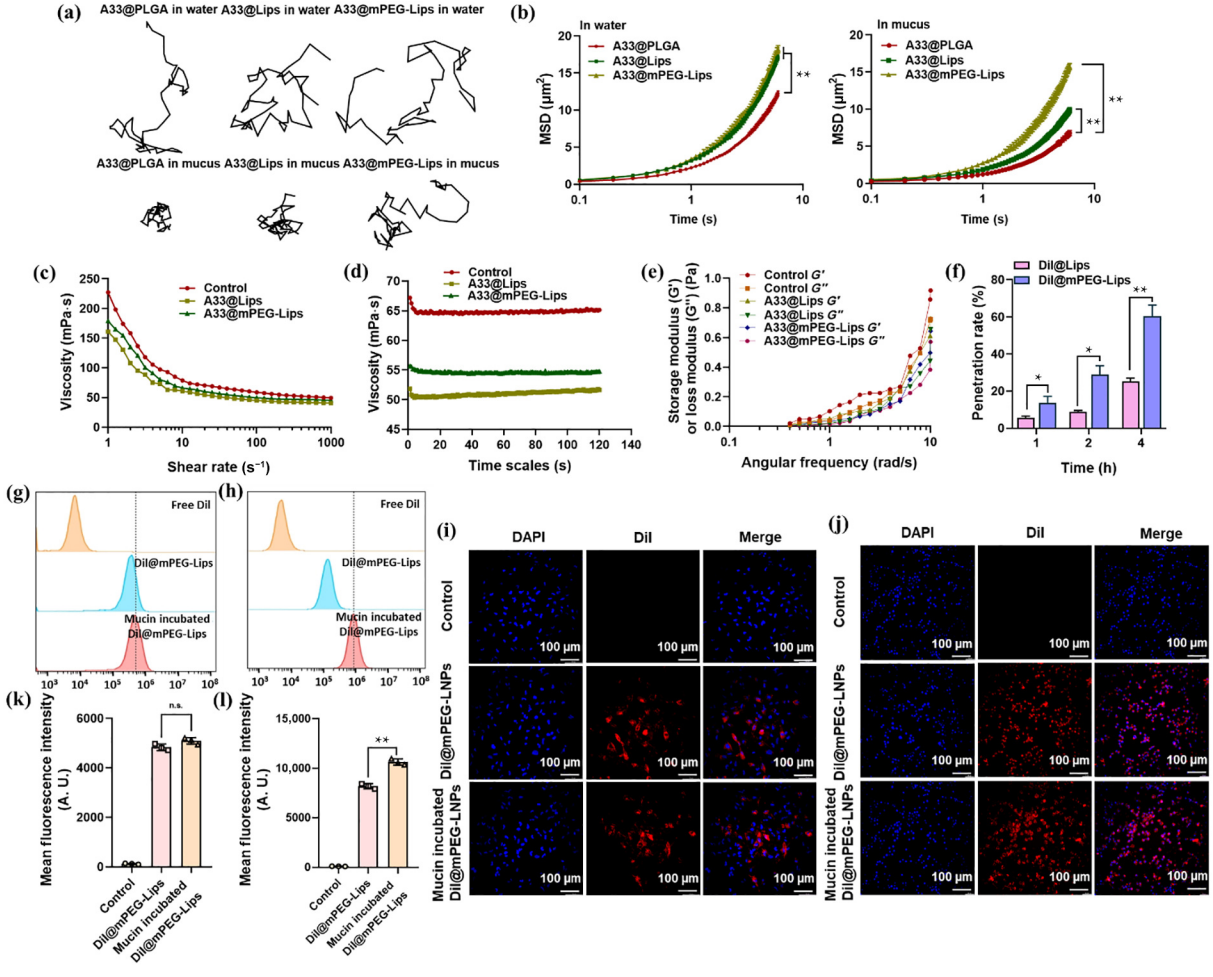

Figure 4 Determination of mucus-penetrating ability of A33-loaded formulations. (a) Representative trajectories of A33-loaded formulations in water and artificial mucus, respectively. (b) Ensemble mean squared displacement of A33-loaded formulations as functions of the time scale (n = 3). (c) The viscosity of artificial mucus as a function of shear rate in the range of 1–103 s^{-1} (n = 3). (d) The viscosity of artificial mucus as a function of time (s) (n = 3). The shear rate is 100 s^{-1}. (e) The relationship between storage modulus (G')/loss modulus (G'') and the angular frequency of artificial mucus (n = 3). All measurements were performed at a strain amplitude of 0.5%. (f) The penetration rate of DiI-labeled various formulations was determined by the Transwell penetration assay (n = 3). The cellular uptake of DiI-labeled various formulations in (g) BEAE-2B and (h) iBMDM cells was analyzed using a flow cytometer. The representative image to observe the cellular uptake of DiI-labeled various formulations in (i) BEAE-2B and (j) iBMDM cells was analyzed using an inverted fluorescence microscope, and further quantitative analysis of the intracellular fluorescence intensity in (k) BEAE-2B and (l) iBMDM cells. *P < 0.05, **P < 0.01, n.s.: not significant.

penetration, and mPEG decoration could significantly improve the particle movement in the mucus solution. Similarly, the effects of the mPEG-DSPE weight ratio on the movement of A33@mPEG-Lips were also evaluated. The data suggested that higher mPEG concentration in Lips improved their movement in mucus (Fig. S8 in the ESM). Based on the comprehensive consideration of the physicochemical properties and mucus penetration performance, we ultimately chose 5% mPEG-DSPE (w/w) for the A33@mPEG-Lips preparation and subsequent studies.

The mucin capture has been reported as the major reason inhibiting the particle penetration. Therefore, the interaction between mucin and formulations was further evaluated by the rheometer. As shown in Figs. 4(c) and 4(d), the viscosity of mucus mixed with normal liposomes and mPEG-decorated liposomes both exhibited a significant decrease in all measured shear rates compared to the control, suggesting that both formulations could interact with mucins and reduce the resistance to deformation of mucus. Compared to the non-decorated liposome group, the mPEG-decorated liposome group exhibited a lower viscosity across the entire investigated shear rate range, indicating that surface modification with mPEG could strongly disrupt the mucin stretching structure and facilitate particle passage through the mucus barrier. The storage modulus (G') and loss modulus (G'') in all investigated groups increased with the oscillatory frequency (Fig. 4(e)). Both G' and G'' of mucus were reduced when mixed with formulations, and the difference between G' and G'' was also reduced, suggesting that the liposomes could effectively reduce the strength of mucus gel with an increased possibility of mucus transformation from gelation to solutions. Compared to the DIR@Lips, DIR@mPEG-Lips exhibited an enhanced mucus disturbance, which is consistent with the particle movement data, indicating a higher mucus penetration ability. The Transwell assay was also applied to investigate the mucus penetration rate of formulations. The mPEG-decorated liposomes demonstrated a notable enhancement in mucus permeation across different time intervals when compared to conventional liposomes. This improvement is attributed to the formation of a hydrophilic surface layer contributed by mPEG, which facilitates better interaction with the mucus barrier and promotes more efficient permeation (Fig. 4(f)). All the above studies validated that PEG-modified liposomes can achieve more rapid and efficient permeation through the pulmonary mucus layer compared to conventional liposomes *in vitro*, providing an effective means for the efficient pulmonary delivery of drugs to epithelial cells.

3.5 Cellular uptake of A33@mPEG-Lips

The cellular uptake of the A33-loaded formulation was analyzed using the flow cytometer and fluorescence inverted microscope in BEAS-2B cells and iBMDM cells. In BEAE-2B cells, there was no significant difference in cellular uptake of Dil@mPEG-Lips whether with or without mucin pre-incubation, suggesting the protein adherent on the particle surface showed no effects in epithelium cellular uptake (Fig. 4(g)). For the iBMDM cells, Dil@mPEG-Lips pre-incubated with mucin exhibited a significantly higher fluorescence signal compared to the mucin non-incubated groups, indicating that improving mucin binding enhances alveolar macrophage-based particle clearance (Fig. 4(h)). The cellular uptake was further analyzed using the inverted fluorescence microscope. Consistent with the flow cytometry data, there was no significant difference in fluorescence signal in BEAS-2B cells for mucin incubated Dil@mPEG-Lips compared to non-incubated formulation (Figs. 4(i) and 4(k)), but that was obviously brighter in iBMDM cells (Figs. 4(j) and 4(l)), suggesting that mPEG-Lips with potential effectively deliver A33 into not only epithelial cells but also alveolar macrophages.

3.6 Therapeutic effects of A33@mPEG-Lips against inflammation and senescence *in vitro*

We further evaluated the anti-senescence ability of A33@mPEG-Lips in senescent BEAS-2B cells. After incubation with A33-loaded formulations, the intracellular expression of SA-β-gal was stained and observed. The SA-β-gal-positive cells were significantly reduced in the A33-formulated groups compared to the senescence model, respectively, indicating the anti-senescence efficacy of the A33-loaded formulations (Figs. 5(a) and 5(b)). Moreover, the A33@mPEG-Lips exhibited slight improvements compared to the A33@Lips groups, which we speculated may be due to the PEG modification reducing the negative charges on the particle surface and thereby reducing the electrostatic repulsion between particles and cell membranes [33]. The SIRT1 expression was also stained and analyzed using the inverted fluorescence microscopy assay. As shown in Figs. 5(c) and 5(d), the fluorescence signal of SIRT1 in aged cells was significantly reduced compared to normal cells. The A33@Lips and A33@mPEG-Lips treatment restored the expression of SIRT1, which prevented the transition of a pro-survival program into a pro-aging mechanism. The pro-inflammatory cytokines (including TGF-β1, TNF-α, IL-1β, and IL-6), which are considered representative SASP secretions, were also determined using an ELISA kit (Fig. 5(e)). Compared to the senescent model group, cells treated with A33-loaded formulations reduced the secretion of SASP and exhibited potential against inflammation and senescence. Similar effects were also observed in senescent iBMDM cells, indicating the potential of A33 in regulating the local immune senescence and inhibiting SASP diffusion (Fig. S9 in the ESM).

The pro-inflammatory cytokines are the primary mediators that promote alveolar macrophage polarization during COPD development, and A33@mPEG-Lips exhibits functions that inhibit inflammatory cytokine activity and scavenge ROS, holding promise for triggering the transition of polarized M1 macrophages into the M2 phenotype. Therefore, we evaluated the expression of surface biomarkers of M2 (CD206) macrophages (Fig. 5(f)). The CSE-induced iBMDM cells exhibited a significant downregulation of CD206, suggesting that the macrophages expressed an M1 phenotype after CSE stimulation. After incubation with A33-loaded liposomes, the expression of these markers was reversed, confirming the anti-inflammatory ability of A33@mPEG-Lips and the repolarization of activated M1 macrophages to the M2 phenotype.

3.7 Biodistribution of A33@mPEG-Lips after pulmonary administration in COPD model mice

Pulmonary deposition and mucus penetration were further evaluated in COPD model mice after administration of free DIR, DIR@Lips, and DIR@mPEG-Lips via intratracheal insufflation (Fig. 6(a)). The mice in different groups were euthanasia followed by an IVIS image of the whole body and major organs at various time intervals after administration (Figs. 6(b)–6(d)). The fluorescence signals were observed primarily in the lungs and persisted for 24 h after administration in the DIR@mPEG-Lips

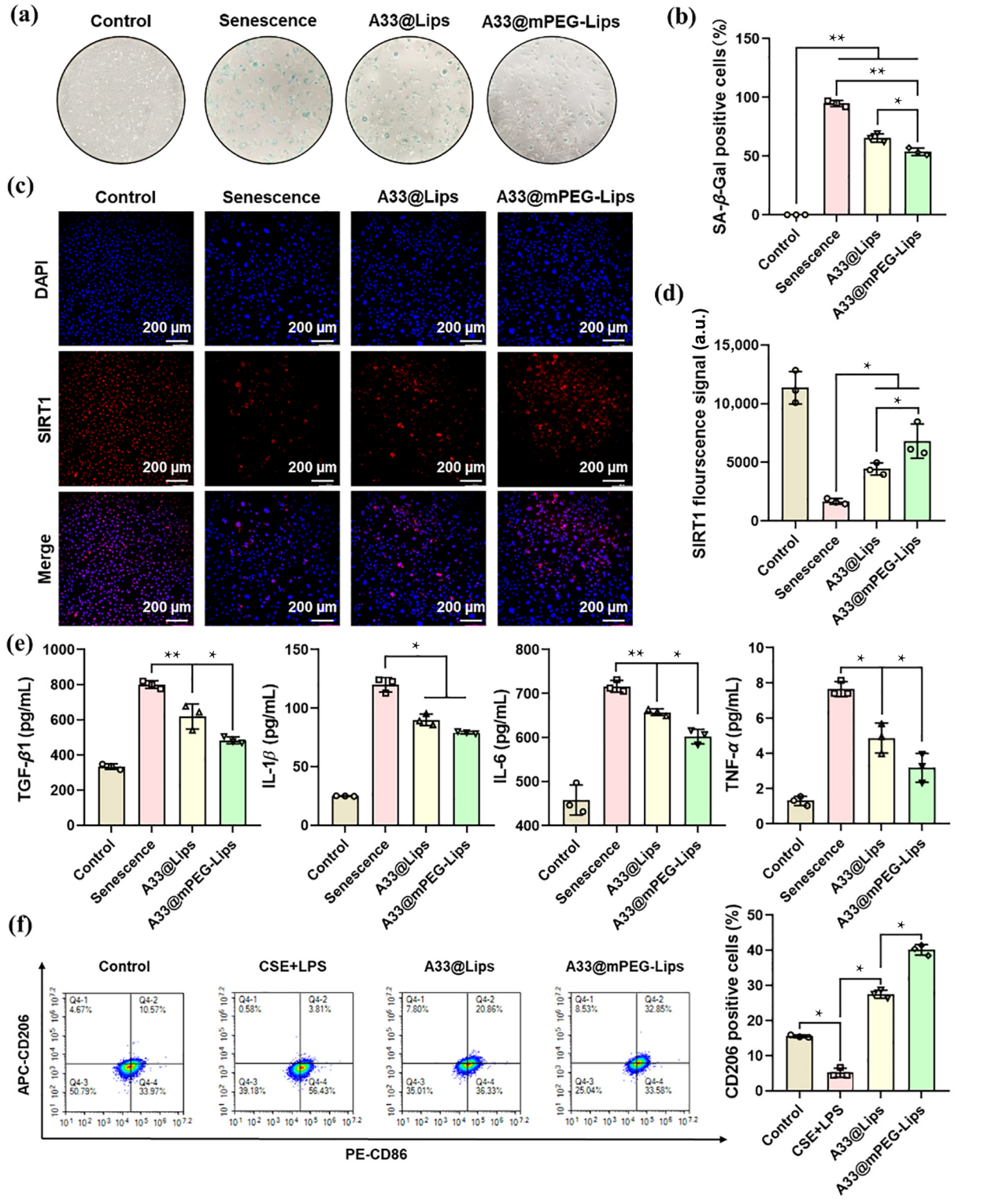

Figure 5 The A33-loaded formulation effectively regulates epithelial cell inflammation and senescence. (a) The representative images of senescent BEAS-2B cells treated with A33-loaded formulations stained by the SA-β-Gal kit, and (b) quantitative analysis of the SA-β-Gal positive cell ratio. (c) The representative images of senescent BEAS-2B cells treated with A33-loaded formulations stained by SIRT1-antibody and (d) quantitative analysis of the SIRT1 fluorescence intensity. (e) The difference in secreted TGF-β1, TNF-α, IL-1β, and IL-6 in senescent BEAS-2B cells treated with A33-loaded formulations. (f) The effects of A33-loaded formulation on the polarizing phenotype of macrophages and proportion of CD206 positive cells (Q1 and Q2 quadrant). $^{*}P < 0.05$, $^{**}P < 0.01$.

groups. While signal intensity rapidly decreased at 6 and 24 h after administration in the free DIR and DIR@Lips groups, which we speculated that was due to their lower mucus penetration ability and high potential for mucin trap, followed by mucociliary escalator-based pulmonary clearance. Therefore, we further prepared the lung tissue section to observe the dye-loaded liposome penetration ability in the respiratory tract. After 24 h of administration, bright DIR fluorescence signals were observed in

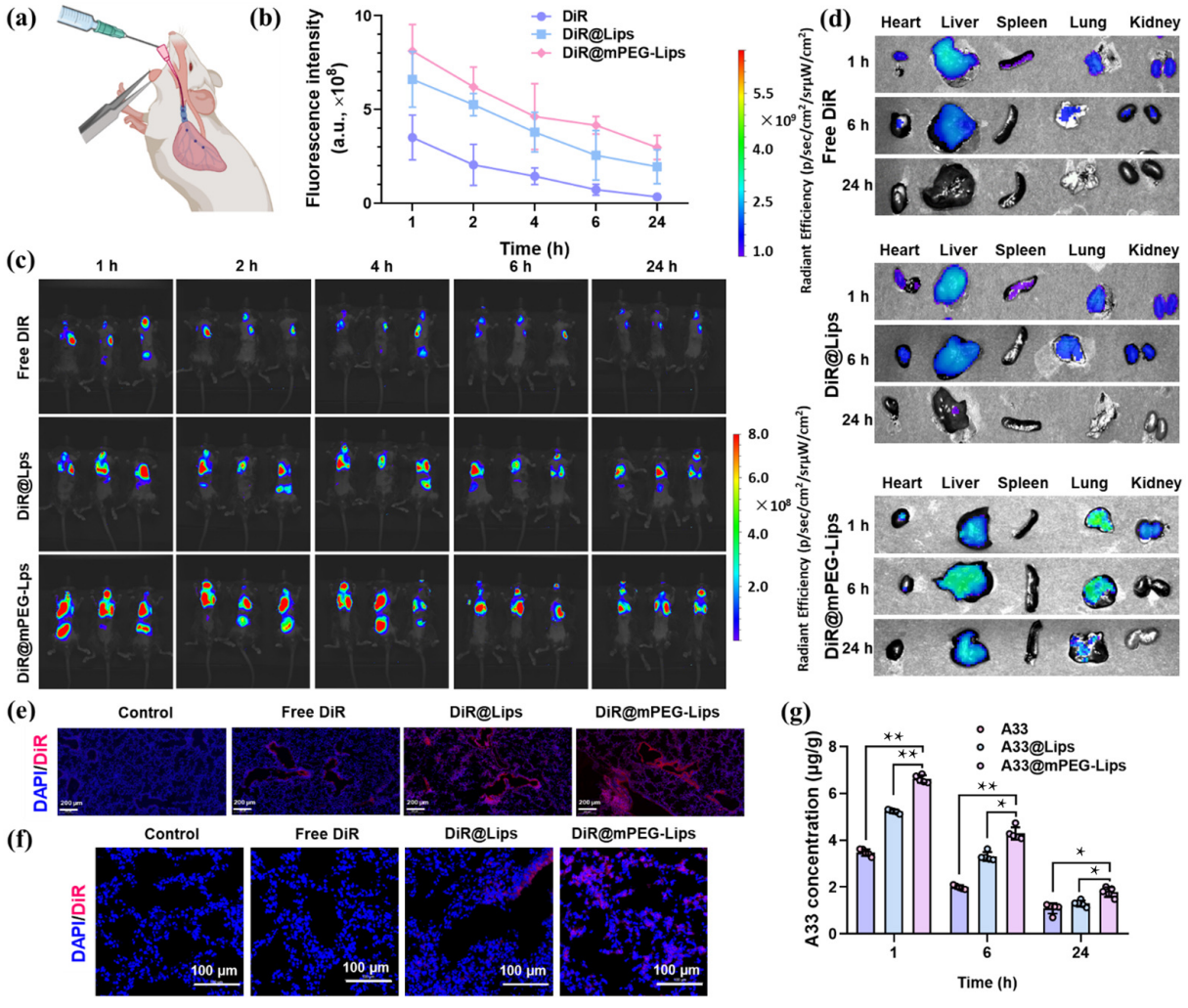

Figure 6 Biodistribution of the A33-loaded liposomes in COPD model mice via intratracheal administration. (a) A schematic illustration of the intratracheal administration for A33-loaded formulation pulmonary administration. The distribution of dye-labeled formulations in COPD model mice was analyzed by calculating (b) the fluorescence intensity from the lung area (n = 3) and observation of representative images of (c) the whole body or (d) isolated major organs at different time intervals. The pulmonary deposition of dye-labeled formulations in lung sections from COPD mice was observed (e) by the inverted fluorescence microscope and (f) by the confocal microscope. (g) The A33 concentration in lung homogenate after intratracheal administration of A33-loaded formulation at different time intervals. $^{*}P < 0.05$, $^{**}P < 0.01$.

the DIR@mPEG-Lips group compared to the other groups using the inverted fluorescence microscope (Fig. 6(e)). A similar result was further observed using confocal microscopy. Limited fluorescence signals of DIR in free dye groups were only observed on the surface layer of epithelial cells surrounding the respiratory tract, indicating that the free dye hardly crossed the mucus layer and reached the epithelial cells. The DIR@Lips group showed an enhanced fluorescence intensity in pulmonary epithelial cells, but the signals were still located near the respiratory tract, suggesting that the normal liposome hardly improves the mucus penetration of loaded drugs. In the DIR@mPEG-Lips group, fluorescence signals were observed in both the surface layer and the deeper regions of the lung epithelia (Fig. 6(f)).

The pulmonary A33 accumulation was also investigated by measuring the drug concentration in lung tissue homogenate after administration (Fig. 6(g)). The A33@mPEG-Lips groups exhibited the highest A33 levels in tissue homogenate, suggesting mPEG decoration improved the mucus permeation and reduced pulmonary clearance compared to free A33 and A33@Lips groups. Moreover, the mPEG decoration forms a hydrophilic coating layer on the liposome surface, which can reduce the absorption of pulmonary surfactant and, consequently, avoid alveolar macrophage phagocytosis. The lower clearance and potential phagocytosis inhibition result in the prolonged retention of A33@mPEG-Lips in the lungs compared to other groups.

3.8 Therapeutic efficacy of A33@mPEG-Lips in COPD model mice

We further evaluated the anti-inflammatory efficiency and senescence inhibitory ability of A33@mPEG-Lips *in vivo*. A smoke-induced COPD mouse model was established (Fig. 7(a)) and confirmed by analyzing the lung tissue structure, followed by determining the polarization of alveolar macrophages. As shown in Fig. 7(b), the alveolar structure was destroyed, with the alveolar walls collapsing and thickening. A large amount of immune cell infiltration was also observed in the H&E slices in the COPD model group. The key biomarkers of alveolar macrophages were further stained, and slices from model groups exhibited an obvious increase

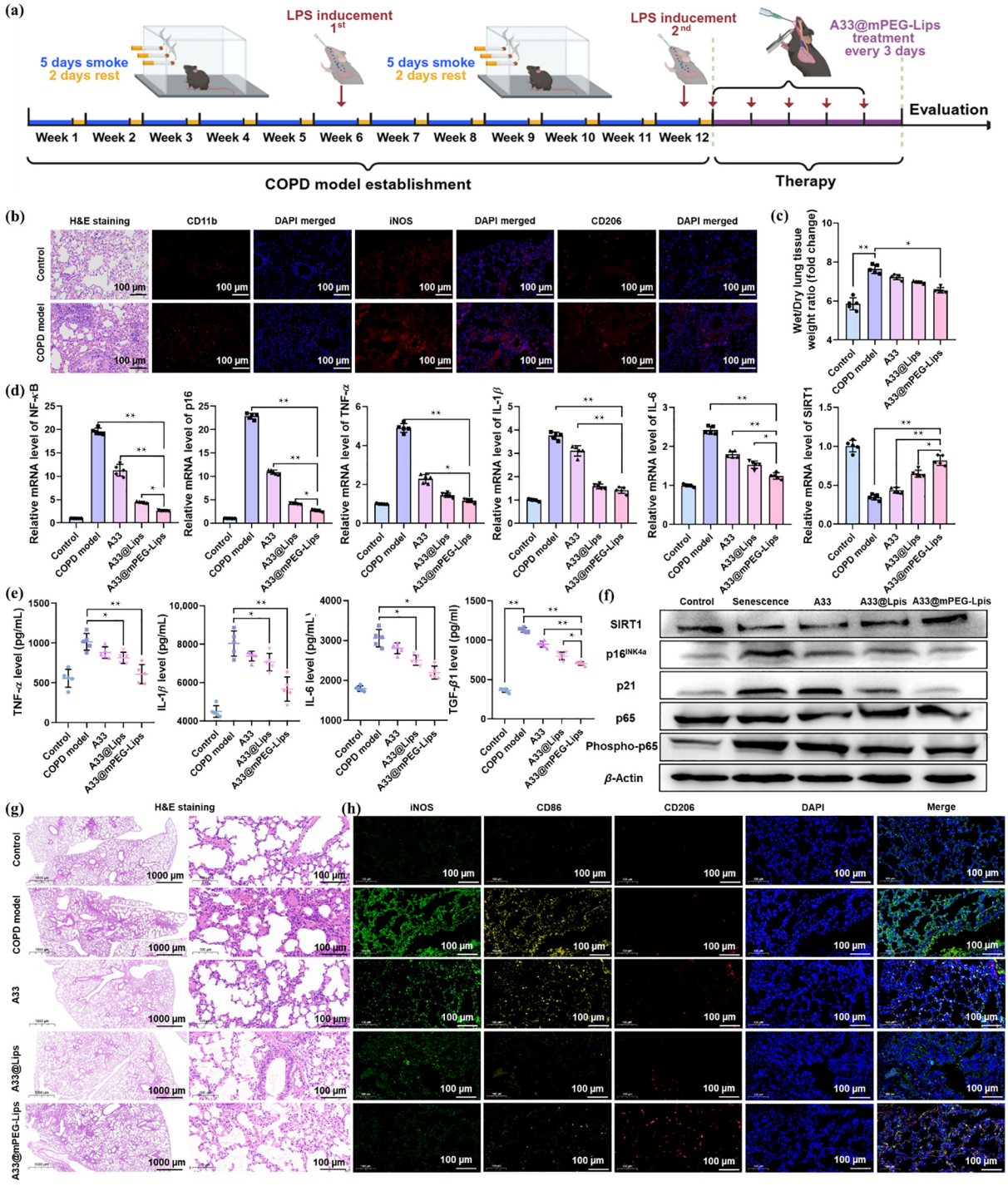

Figure 7 The therapeutic efficiency of A33 in inhibition of pulmonary chronic inflammation. (a) The scheme diagram of COPD mouse model establishment and A33-loaded formulation treatment via intratracheal insufflation. (b) The cigarette-induced mouse model was confirmed by pathological section H&E staining and macrophage polarization analysis of the isolated lungs. (c) The wet-to-dye ratio of lung tissues (n = 5), (d) expression of inflammatory-related regulators at mRNA levels in lung homogenates (n = 5), (e) secreted pro-inflammatory cytokines in BALF, and (f) biomarkers of senescence at the protein level in lung homogenates were isolated from different A33-treated COPD model mice and analyzed. Representative images of the pulmonary pathological section were stained with (g) H&E and (h) macrophage polarization markers. $^{*}P < 0.05$, $^{**}P < 0.01$.

in CD11b and iNOS signals but similar CD206 signals, suggesting the polarization of alveolar macrophages to an M1 phenotype in the lungs of COPD model mice.

After treatment with A33-loaded formulations, the lung wet-to-dry ratio was calculated and used to assess the treatment outcome. A33@mPEG-Lips most effectively reduced the pulmonary edema-induced wet/dry weight ratio (Fig. 7(c)). Meanwhile, the expression of key inflammatory regulators and cytokines was evaluated at the mRNA level (Fig. 7(d)). NF-κB, as the key regulator of major pro-inflammatory signaling pathways, was significantly reduced after A33@mPEG-Lips treatment and exhibited a four-fold decrease compared to the COPD model group, the A33 alone group, and the

A33@Lips group, respectively. The major types of cytokines, such as IL-6, IL-1β, and TNF-α, were also reduced most in the A33@mPEG-Lips group, indicating that the inhibition of NF-κB could further reduce the expression of inflammatory cytokines. Meanwhile, the secretion of the above pro-inflammatory cytokines was further confirmed in the protein levels after treatment (Fig. 7(e)). Consistent with the trend in mRNA level, the secretion of cytokines such as TNF-α, IL-1β, IL-6, and TGF-β1 was reduced in BALF after treatment. The expression of inflammatory and senescence regulators was also analyzed using the western blot assay (Fig. 7(f) and Fig. S10 in the ESM). A33@mPEG-Lips treatment reduced the intracellular protein levels of NF-κB (p65), $p16^{INK4a}$, and p21 but improved the SIRT1 protein level, confirming that A33 treatment inhibited the inflammatory maintenance and senescence-regulating ability.

The *in vivo* anti-inflammatory efficacy of the A33-loaded formulation was also analyzed via pathological section staining analysis. After treatment with A33@mPEG-Lips, the edema in the lungs was significantly alleviated, with normalization of the alveolar wall (Fig. 7(g)). The phenotypes of alveolar macrophages in the lungs were further evaluated by staining iNOS, CD86, and CD206 in lung sections (Fig. 7(h) and Fig. S11 in the ESM). The fluorescence signals of CD206 (Red) were significantly elevated and accompanied by decreased iNOS signals (Green) in A33@mPEG-Lips compared to other treatment groups, suggesting that the PDE4B inhibitor could effectively regulate macrophage repolarization and transition to an anti-inflammatory M2 phenotype.

The anti-senescent potential of the A33-loaded formulation was also evaluated by analyzing the expression of key regulators and SASP secretion. The expression of senescent biomarkers, such as p16 and p21, was decreased, but SIRT1 levels increased in the treatment groups, confirming the potential of A33 in anti-senescence treatment (Fig. 7(d)). The protein levels were also determined and showed a similar trend (Fig. 7(f)). The expression of SA-β-gel and Lamin B1, both senescent biomarkers, was significantly reduced (SA-β-gel) or enhanced (Lamin B1) after A33@mPEG-Lips treatment, respectively (Figs. 8(a) and 8(b)). The restored expression of SIRT1 and Ki67 (proliferation marker) (Figs. 7(f) and 8(c)) combined with reduced expression of SASP, such as TNF-α, IL-1β, IL-6, TGF-β1, and MMP12 (Figs. 7(e) and 8(d)), consistently confirms that A33 could inhibit the cell aging in the COPD lungs.

3.9 Safety evaluation

The *in vitro* cytotoxicity of A33@mPEG-Lips was evaluated in both BEAS-2B cells and iBMDM cells. The data suggested that only limited cytotoxicity was observed for A33@mPEG-Lips when the concentration of A33 exceeded 37.5 μM, which was significantly higher than the pre-clinical application concentration (Fig. 9(a)). Similar data were observed in iBMDM cells, indicating the acceptable safety of A33@mPEG-Lips (Fig. 9(b)). The ALT and AST levels in serum were not significantly different before and after administration (Figs. 9(c) and 9(d)), indicating that no liver toxicity was associated with the formulation after pulmonary administration. Moreover, the safety of A33@mPEG-Lips was investigated by examining the H&E pathological section of various organs. Data exhibited no significant difference in the major organs after pulmonary administration of A33@mPEG-Lips compared to the control groups, indicating no systemic toxicity of the formulation and suggesting it is relatively safe for COPD treatment application (Fig. 9(e)).

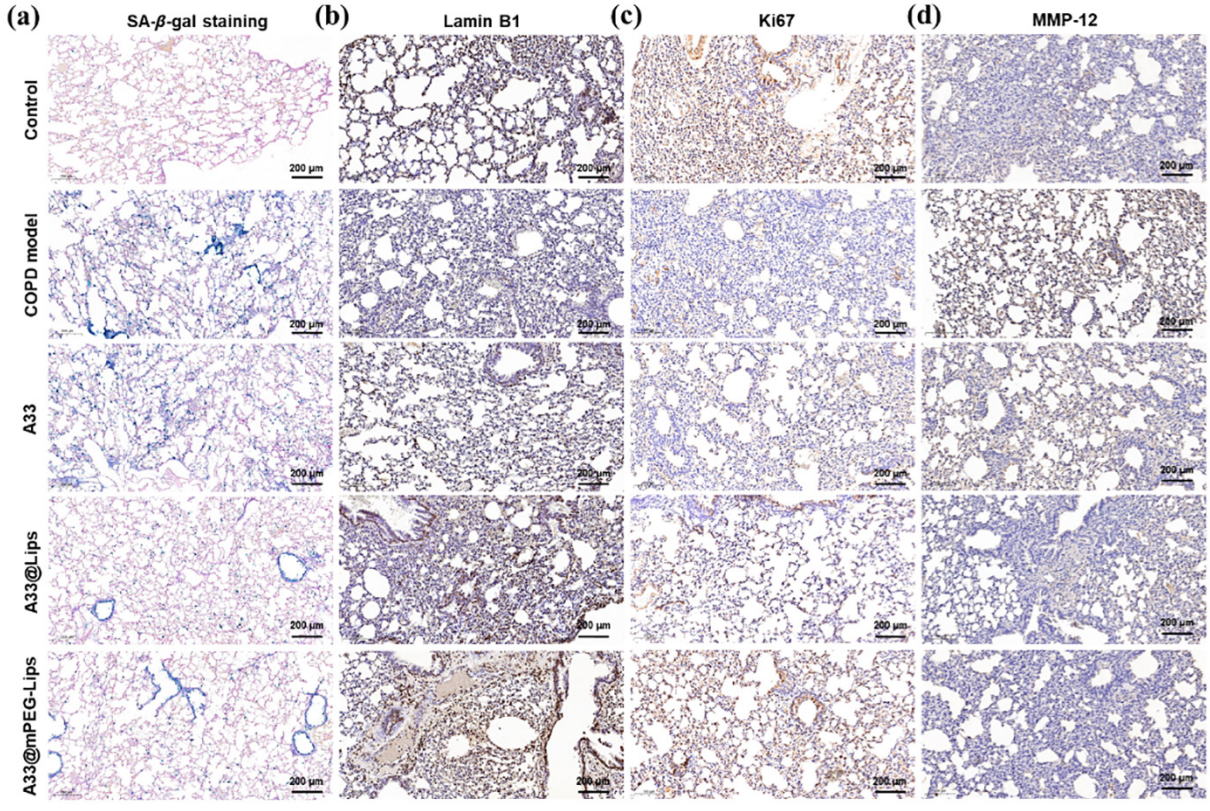

Figure 8 The effects of A33 in the regulation of pulmonary cellular senescence. Representative images of the pulmonary pathological section were stained with (a) SA-β-gal, (b) Lamin B1, (c) Ki67, and (d) MMP-12.

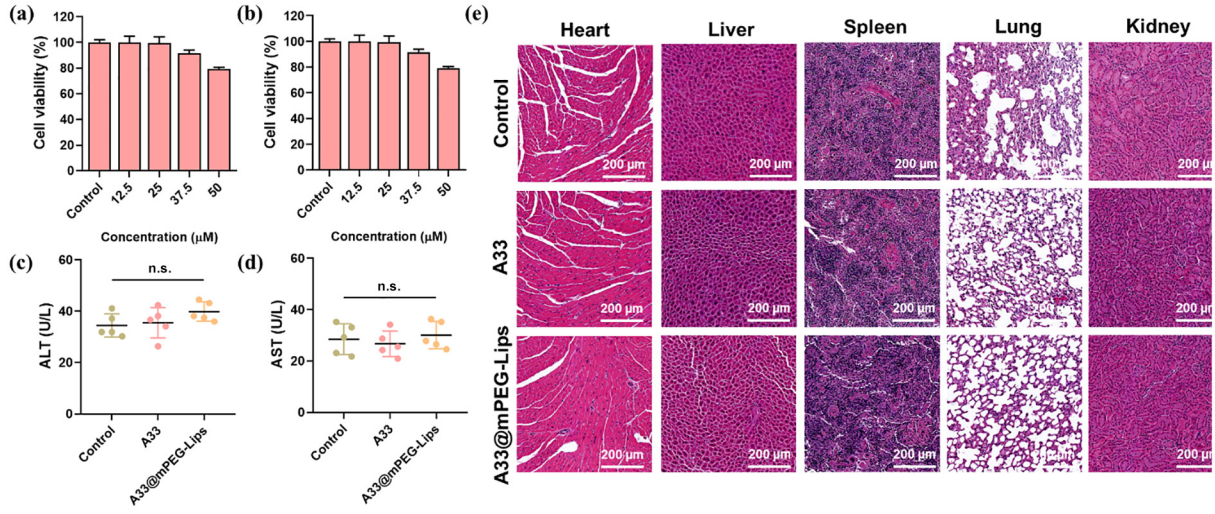

Figure 9 Safety evaluation of A33@mPEG-Lips *in vitro* and *in vivo*. The cytotoxicity of A33@mPEG-Lips on (a) BEAS-2B and (b) iBMDM cells at different concentrations, respectively (n = 6). The serum (c) ALT and (d) AST levels in healthy mice after repeated administration of A33@mPEG-Lips. (e) The major organs are stained by H&E. n.s.: not significant.

4 Discussion

Double or triple treatment strategies have been developed and applied in COPD clinical treatment to alleviate airflow obstruction, but still no improvement in delayed respiratory tissue function deterioration. Strategies to inhibit chronic inflammation and remove detrimental senescent cells from the lungs of patients with COPD are gaining interest in pre-clinical investigations.

The imbalance between oxidation and antioxidation has been considered closely related to the occurrence and development of COPD [34]. Cigarette smoke contains plenty of oxidants that could directly damage the respiratory epithelium and cause extra mucus secretion, extracellular matrix remodeling, DNA damage, etc., which leads to epithelial cell death and induces a protracted local inflammatory microenvironment. Moreover, the extra-secreted pro-inflammatory cytokines could also recruit and activate immune cells, such as alveolar macrophages, to destroy the damaged epithelial cells, further exacerbating the inflammatory environment. Long-term local inflammation has been considered the major reason for inducing COPD generation, progression, and accelerating lung aging [35]. Accordingly, potential COPD therapeutic strategy development has been oriented towards effectively inhibiting local inflammation and repairing pulmonary senescence.

The second messenger, cAMP, has been recognized as an inducer of anti-inflammatory responses, and cAMP-dependent pathways have been extensively exploited pharmacologically to treat inflammatory diseases. Elevated cAMP levels could not only inhibit the biosynthesis and release of inflammatory cytokines and chemokines, but also suppress T cell activation and regulate the functions of macrophages and neutrophils, contributing to the development of bronchiectasis. PDE4 is a cAMP-specific enzyme that can convert the second messenger cAMP into 5'-AMP, thereby reducing intracellular cAMP levels [8]. The anti-inflammatory effects of PDE4 inhibitors make them a promising therapeutic target for increasing intracellular cAMP levels, thereby relaxing airway smooth muscle and inhibiting hyperactive chronic inflammation. However, marketed universal PDE4 inhibitors, such as roflumilast, administered orally, show anti-inflammatory ability by inhibiting all PDE4 subtypes and reducing NF-κB activation. Nevertheless, they face systemic side effects, including nausea, headache, and insomnia, which are mainly due to the inhibition of the PDE4D subtype. Therefore, novel PDE4 inhibitors are urgently needed to be developed for selective inhibition of PDE4B. A33, as a PDE4B inhibitor, exhibited a highly selective (IC_{50} of 15 nM for PDE4B and IC_{50} of about 1.7 μM for PDE4D) and was therefore being considered a potential anti-inflammation agent for COPD treatment in our investigation [36].

Meanwhile, the administration route may also affect the formulation efficiency and compliance. PDE4B is the predominant phosphodiesterase subtype expressed in inflammatory area and immune cells within the respiratory tract, and its selective inhibition is considered sufficient to achieve potent anti-inflammatory effects. In contrast, inhibition of other PDE4 subtypes using the pan-PDE4 inhibitors, particularly PDE4D, has been strongly associated with dose-limiting systemic adverse effects such as nausea and emesis, which contributed to the serious adverse reaction of roflumilast [37]. Therefore, A33, as a PDE4B-selective inhibitor, offers the potential to retain the desired anti-inflammatory efficacy while markedly reducing off-target toxicity. Moreover, pulmonary delivery of a PDE4B inhibitor not only achieves high drug concentrations at the disease site with limited systemic exposure, further minimizing the risk of systemic side effects commonly observed with orally administered pan-PDE4 inhibitors, but also reduces the treatment dosage and frequency. Therefore, it should be the most suitable administration route for COPD therapy. In this research, we aimed to formulate A33 as the liposome inhalation solution. The A33 could be effectively encapsulated inside the liposome with a drug loading of 7.31% ± 0.17% and an acceptable encapsulation efficiency. The A33-loaded liposome exhibited acceptable physicochemical properties, drug release behavior, and atomization stability, indicating that the A33-loaded liposome inhalation solution is suitable for pulmonary administration.

Effective pulmonary delivery needs to overcome several physiological barriers. The deposition of atomized particles is primarily influenced by the aerodynamic diameter of the particles, which should be within the range of 0.5 to 5 μm [38]. The NGI investigation suggested that A33@mPEG-Lips has an MMAD of 2.71 μm when atomized using an inhalation device, which could

achieve efficient pulmonary deposition. Furthermore, the deposited particles must cross the sticky mucus layer to be taken up by epithelial cells. The secreted glycoprotein chains in the mucus layer can crosslink to form a porous, gel-like structure, thereby restricting the passage of foreign particles through electrostatic and hydrophobic interactions [39]. The surface decoration was reported as the most effective way to enhance the mucus penetration of particles, and we utilized DSPE-PEG to improve the hydrophilicity of the A33-loaded formulation.

The PEG coating forms a hydrated steric barrier that minimizes adhesive and electrostatic interactions with mucins, thereby facilitating particle transport and retention within the airway environment. For example, Kim et al. engineered PEGylated lipid nanoparticles for inhalable mRNA delivery and demonstrated that the PEG coating significantly optimized particle stability and penetration through the mucus barrier, thereby promoting more efficient cellular uptake and gene expression in the lung environment [39]. Similarly, Osman et al. developed PEGylated, enhanced cell-penetrating peptide nanoparticles for lung gene delivery, in which PEGylation not only mitigated excessive interactions with mucus glycoproteins but also facilitated deeper tissue penetration and transfection efficiency [40]. All the studies supported that PEG surface functionalization is a key strategy for designing efficient nanoparticle-based delivery systems for COPD treatment. Our preliminary data suggested that with the increase of DSPE-PEG, the penetration of the formulation significantly increased. Considering safety and biodegradability, we select to add 5% (w/w) of DSPE-PEG to prepare the A33@mPEG-Lips. The movement trajectories and penetration rates in artificial mucus all demonstrate that mPEG modification can effectively enhance the transport of A3-loaded formulations into epithelial cells and macrophages.

We further evaluated the anti-inflammatory and anti-senescence ability of A33@mPEG-Lips in a smoke-induced COPD mouse model. The oxidation stress induced by cigarette smoke directly damaged epithelial cells by inducing cell apoptosis and senescence, followed by an inflammatory microenvironment. The inflammatory cytokines can recruit immune cells and exacerbate local inflammation, thereby further accelerating the remodeling or senescence of damaged tissue. A33, as a potential inflammation regulator, inhibited intracellular NF-κB activation and the secretion of downstream cytokines into BALF. Moreover, the anti-inflammatory-induced repolarization of alveolar macrophages enhanced the expression of the M2-like phenotype. The SASP secretion and senescence markers were further reduced after treatment, indicating the potential of PDE4B inhibitors in regulating pulmonary aging and improving lung function.

5 Conclusions

Oxidant-induced long-term imbalance of intracellular oxidative stress is the primary factor leading to local chronic inflammatory formation, which further damages pulmonary function and contributes to the development of COPD by accelerating the aging of the respiratory system. Pulmonary delivery of A33, a highly selective PDE4B inhibitor, resulted in effective inflammatory regulation with minimal side effects, indicating potential for the treatment of COPD. Therefore, we designed a PEG-decorated liposome inhalation solution to overcome the special airway physiological structure and existing mucus barrier, thereby achieving effective pulmonary delivery of A33. A33-loaded liposomes with PEG decoration successfully inhibited inflammation intensification in a COPD mouse model and exhibited potential in blocking the senescence process of epithelial cells, indicating their extraordinary treatment efficiency in inflammatory hyperactivity-induced pulmonary local disease.

Electronic Supplementary Material: Supplementary material (the quantitative analysis of the Western blot bands at cellular level; formulation optimization and preparing process optimization of liposomes by single-factor prescription; effects of mPEG decoration on the characteristics of drug-loaded liposomes; stability evaluation of blank liposomes and drug loaded liposomes; the effects of mPEG modification on mucus-penetrating ability; the formulation regulates SASP secretion in senescent iBMDM cells; the quantitative analysis of the Western blot band at animal level; and the semi-quantitative data of fluorescence intensity signals in immunohistochemical sections) is available in the online version of this article at https://doi.org/10.26599/NR.2026.94908499.

Data availability

All data needed to support the conclusions in the paper are presented in the manuscript and/or the Electronic Supplementary Material. Additional data related to this paper may be requested from the corresponding author upon request.

Acknowledgements

This work was supported by the National Natural Science Foundation of China (Nos. 32301178 and 32371444), the Natural Science Foundation of Jiangsu Province (No. BK20230316), the Natural Science Foundation of Jiangsu Province-Outstanding Youth Foundation (No. BK20220102), the Natural Science Foundation of the Jiangsu Higher Education Institutions of China (No. 23KJB350003), and Natural Science Foundation of Fujian Province of China (No. 2025J01706). This work is also supported by the Discipline Fund of the School of Pharmacy from Nanjing Tech University (No. 202303), NMPA Key Laboratory for Research and Evaluation of Pharmaceutical Preparations and Excipients and Department of Pharmaceutics (No. PPE2023002), and Fujian Key Laboratory of Natural Medicine Pharmacology (No. FJNMP-202401). The graphical abstract and scheme diagram in Fig. 7 were produced using Biorender.com.

Declaration of competing interest

All the contributing authors report no conflict of interests in this work.

Author contribution statement

Q. Y. W.: Writing – original draft, supervision, project administration, funding acquisition, conceptualization. X. M. L.: Supervision, conceptualization. H. R.: Writing – original draft, supervision, funding acquisition, conceptualization. Z. J. M.: Supervision, conceptualization. C. G. G.: Project administration, methodology, formal analysis, data curation. C. T.: Project administration, methodology, formal analysis, data curation. R. J. S.: Software, formal analysis. R. T. Z.: Software, formal analysis. J. N. M.: Software, formal analysis. Q. H. D.: Software, formal analysis. All authors discussed the results and commented on the manuscript.

Informed consent

Not applicable.

Ethics statement

All animal experiments were approved by the Animal Care and Use Committee of Nanjing Tech University (No. 20230304-04).

Use of AI statement

None.

References

[1] Adeloye, D.; Song, P. G.; Zhu, Y. J.; Campbell, H.; Sheikh, A.; Rudan, I.; NIHR RESPIRE Global Respiratory Health Unit. Global, regional, and national prevalence of, and risk factors for, chronic obstructive pulmonary disease (COPD) in 2019: A systematic review and modelling analysis. *Lancet Respir. Med.* **2022**, *10*, 447–458.

[2] Riley, C. M.; Sciurba, F. C. Diagnosis and outpatient management of chronic obstructive pulmonary disease: A review. *JAMA* **2019**, *321*, 786–797.

[3] He, Y. X.; Qian, D. C.; Diao, J. A.; Cho, M. H.; Silverman, E. K.; Gusev, A.; Manrai, A. K.; Martin, A. R.; Patel, C. J. Prediction and stratification of longitudinal risk for chronic obstructive pulmonary disease across smoking behaviors. *Nat. Commun.* **2023**, *14*, 8297.

[4] Li, X.; Li, C. T.; Zhang, W. Y.; Wang, Y. N.; Qian, P. X.; Huang, H. Inflammation and aging: Signaling pathways and intervention therapies. *Signal Transduct. Target. Ther.* **2023**, *8*, 239.

[5] Jin, J.; Mu, Y. M.; Zhang, H. M.; Sturmlechner, I.; Wang, C. Y.; Jadhav, R. R.; Xia, Q.; Weyand, C. M.; Goronzy, J. J. CISH impairs lysosomal function in activated T cells resulting in mitochondrial DNA release and inflammaging. *Nat. Aging* **2023**, *3*, 600–616.

[6] Wang, B. S.; Han, J.; Elisseeff, J. H.; Demaria, M. The senescence-associated secretory phenotype and its physiological and pathological implications. *Nat. Rev. Mol. Cell Biol.* **2024**, *25*, 958–978.

[7] Singh, D.; Lea, S.; Mathioudakis, A. G. Inhaled phosphodiesterase inhibitors for the treatment of chronic obstructive pulmonary disease. *Drugs* **2021**, *81*, 1821–1830.

[8] Xing, Y. J.; Hou, Y. F.; Fan, T. F.; Gao, R.; Feng, X. H.; Li, B. L.; Pang, J. L.; Guo, W. J.; Shu, T.; Li, J. Q. et al. Endothelial phosphodiesterase 4B inactivation ameliorates endothelial-to-mesenchymal transition and pulmonary hypertension. *Acta Pharm. Sin. B* **2024**, *14*, 1726–1741.

[9] Shi, J. Y.; Song, C. H.; Zhang, P. G.; Wang, J.; Huang, W. Y.; Yu, T.; Wei, Z. J.; Wang, L. F.; Zhao, L. X.; Zhang, R. et al. Microglial circDlg1 modulates neuroinflammation by blocking PDE4B ubiquitination-dependent degradation associated with Alzheimer's disease. *Theranostics* **2025**, *15*, 3401–3423.

[10] Li, X. M.; Li, W. J.; Zang, C. C.; Yan, J. J.; Cai, M.; Liu, Z. Z.; Cai, R. L.; Gao, Y.; Qi, Y. Hua-Shi-Bai-Du decoction inactivates NLRP3 inflammasome through inhibiting PDE4B in macrophages and ameliorates mouse acute lung injury. *Phytomedicine* **2024**, *134*, 155985.

[11] Naganuma, K.; Omura, A.; Maekawara, N.; Saitoh, M.; Ohkawa, N.; Kubota, T.; Nagumo, H.; Kodama, T.; Takemura, M.; Ohtsuka, Y. et al. Discovery of selective PDE4B inhibitors. *Bioorg. Med. Chem. Lett.* **2009**, *19*, 3174–3176.

[12] De Savi, C.; Cox, R. J.; Warner, D. J.; Cook, A. R.; Dickinson, M. R.; McDonough, A.; Morrill, L. C.; Parker, B.; Andrews, G.; Young, S. S. et al. Efficacious inhaled PDE4 inhibitors with low emetic potential and long duration of action for the treatment of COPD. *J. Med. Chem.* **2014**, *57*, 4661–4676.

[13] Sudduth, E. R.; Trautmann-Rodriguez, M.; Gill, N.; Bomb, K.; Fromen, C. A. Aerosol pulmonary immune engineering. *Adv. Drug Deliv. Rev.* **2023**, *199*, 114831.

[14] Guo, Y.; Bera, H.; Shi, C. Z.; Zhang, L.; Cun, D.; Yang, M. S. Pharmaceutical strategies to extend pulmonary exposure of inhaled medicines. *Acta Pharm. Sin. B* **2021**, *11*, 2565–2584.

[15] Kumari, A.; Pal, S.; G, B. R.; Mohny, F. P.; Gupta, N.; Miglani, C.; Pattnaik, B.; Pal, A.; Ganguli, M. Surface-engineered mucus penetrating nucleic acid delivery systems with cell penetrating peptides for the lungs. *Mol. Pharm.* **2022**, *19*, 1309–1324.

[16] Li, Z. B.; Luo, G. H.; Hu, W. P.; Hua, J. L.; Geng, S. Y.; Chu, P. K.; Zhang, J.; Wang, H. Y.; Yu, X. F. Mediated drug release from nanovehicles by black phosphorus quantum dots for efficient therapy of chronic obstructive pulmonary disease. *Angew. Chem., Int. Ed.* **2020**, *59*, 20568–20576.

[17] Huck, B. C.; Murgia, X.; Frisch, S.; Hittinger, M.; Hidalgo, A.; Loretz, B.; Lehr, C. M. Models using native tracheobronchial mucus in the context of pulmonary drug delivery research: Composition, structure and barrier properties. *Adv. Drug Deliv. Rev.* **2022**, *183*, 114141.

[18] Wang, Y.; Zhang, J.; Liu, Y.; Yue, X.; Han, K.; Kong, Z. C.; Dong, Y. M.; Yang, Z. M.; Fu, Z. P.; Tang, C. W. et al. Realveolarization with inhalable mucus-penetrating lipid nanoparticles for the treatment of pulmonary fibrosis in mice. *Sci. Adv.* **2024**, *10*, eado4791.

[19] Ma, Y. B.; Guo, Y. Y.; Liu, S.; Hu, Y.; Yang, C.; Cheng, G.; Xue, C. Y.; Zuo, Y. Y.; Sun, B. B. pH-mediated mucus penetration of zwitterionic polydopamine-modified silica nanoparticles. *Nano Lett* **2023**, *23*, 7552–7560.

[20] Hu, H. Q.; Hua, S. Y.; Lu, F.; Zhang, W. T.; Zhang, Z. W.; Cui, J. R.; Lei, X. Y.; Xia, J. Y.; Xu, F.; Zhou, M. Mucous permeable nanoparticle for inducing cuproptosis-like death in broad-spectrum bacteria for nebulized treatment of acute pneumonia. *Adv. Sci.* **2025**, *12*, 2408580.

[21] Hua, S. Y.; Hu, H. Q.; Liu, J.; Lu, F.; Yu, R. C.; Zhang, X. N.; Sun, H. M.; Wang, Z. W.; Li, Y. G.; Xia, J. Y. et al. A mucous permeable local delivery strategy based on manganese-enhanced bacterial cuproptosis-like death for bacterial pneumonia treatment. *ACS Nano* **2024**, *18*, 31923–31940.

[22] Chen, Y. M.; Lin, S. S.; Wang, L.; Zhang, Y. F.; Chen, H.; Fu, Z. Z.; Zhang, M. M.; Luo, H. L.; Liu, J. Y. Reinforcement of the intestinal mucosal barrier via mucus-penetrating PEGylated bacteria. *Nat. Biomed. Eng.* **2024**, *8*, 823–841.

[23] Guo, Y. Y.; Ma, Y. B.; Chen, X.; Li, M.; Ma, X. H.; Cheng, G.; Xue, C. Y.; Zuo, Y. Y.; Sun, B. B. Mucus penetration of surface-engineered nanoparticles in various pH microenvironments. *ACS Nano* **2023**, *17*, 2813–2828.

[24] He, Z. J.; Huang, B. Q.; Cai, L. H. Bottlebrush polyethylene glycol nanocarriers translocate across human airway epithelium via molecular architecture-enhanced endocytosis. *ACS Nano* **2024**, *18*, 17586–17599.

[25] Li, H. Y.; Granger, L.; Raimi-Abraham, B. T.; Shattock, R. J.; Makatsoris, C.; Forbes, B. Pulmonary delivery of LNP-mRNAs aerosolised by vibrating mesh nebulizer: An emphasis on variations and in-depth analyses of physicochemical properties. *Int. J. Pharm.* **2025**, *680*, 125796.

[26] Luo, L. J.; Li, T.; Zeng, Z. H.; Li, H. R.; He, X.; Chen, Y. CSE reduces OTUD4 triggering lung epithelial cell apoptosis via PAI-1 degradation. *Cell Death Dis.* **2023**, *14*, 614.

[27] Tsai, L. H.; Young, T. H.; Yen, C. H.; Yao, W. C.; Chang, C. H. Intratumoral thermo-chemotherapeutic alginate hydrogel containing doxorubicin loaded PLGA nanoparticle and heating agent. *Int. J. Biol. Macromol.* **2023**, *251*, 126221.

[28] Sharma, A.; Vaghasiya, K.; Gupta, P.; Singh, A. K.; Gupta, U. D.; Verma, R. K. Dynamic mucus penetrating microspheres for efficient pulmonary delivery and enhanced efficacy of host defence peptide (HDP) in experimental tuberculosis. *J. Control. Release* **2020**, *324*, 17–33.

[29] Xu, H.; Ling, M.; Xue, J. C.; Dai, X. Y.; Sun, Q.; Chen, C.; Liu, Y.; Zhou, L.; Liu, J. P.; Luo, F. et al. Exosomal microRNA-21 derived from bronchial epithelial cells is involved in aberrant epithelium-fibroblast cross-talk in COPD induced by cigarette smoking. *Theranostics* **2018**, *8*, 5419–5433.

[30] Wang, Q. Y.; Mi, G. J.; Hickey, D.; Li, Y. N.; Tu, J. S.; Webster, T. J.; Shen, Y. Azithromycin-loaded respirable microparticles for targeted pulmonary delivery for the treatment of pneumonia. *Biomaterials* **2018**, *160*, 107–123.

[31] Faraonio, R. Oxidative stress and cell senescence process. *Antioxidants* **2022**, *11*, 1718.

[32] Hashizaki, K.; Taguchi, H.; Itoh, C.; Sakai, H.; Abe, M.; Saito, Y.; Ogawa, N. Effects of poly(ethylene glycol) (PEG) chain length of PEG-lipid on the permeability of liposomal bilayer membranes. *Chem. Pharm. Bull.* **2003**, *51*, 815–820.

[33] Suk, J. S.; Xu, Q. G.; Kim, N.; Hanes, J.; Ensign, L. M. PEGylation as a strategy for improving nanoparticle-based drug and gene delivery. *Adv. Drug Deliv. Rev.* **2016**, *99*, 28–51.

[34] Forman, H. J.; Zhang, H. Q. Targeting oxidative stress in disease: Promise and limitations of antioxidant therapy. *Nat. Rev. Drug Discov.* **2021**, *20*, 689–709.

[35] Chung, H. Y.; Kim, D. H.; Lee, E. K.; Chung, K. W.; Chung, S.; Lee, B.; Seo, A. Y.; Chung, J. H.; Jung, Y. S.; Im, E. et al. Redefining chronic inflammation in aging and age-related diseases: Proposal of the senoinflammation concept. *Aging Dis.* **2019**, *10*, 367–382.

[36] Schepers, M.; Paes, D.; Tiane, A.; Rombaut, B.; Piccart, E.; van Veggel, L.; Gervois, P.; Wolfs, E.; Lambrichts, I.; Brullo, C. et al. Selective PDE4 subtype inhibition provides new opportunities to intervene in neuroinflammatory versus myelin damaging hallmarks of multiple sclerosis. *Brain Behav. Immun.* **2023**, *109*, 1–22.

[37] Beghè, B.; Rabe, K. F.; Fabbri, L. M. Phosphodiesterase-4 inhibitor therapy for lung diseases. *Am. J. Respir. Crit. Care Med.* **2013**, *188*, 271–278.

[38] Chang, R. Y. K.; Chan, H. K. Advancements in particle engineering for inhalation delivery of small molecules and biotherapeutics. *Pharm. Res.* **2022**, *39*, 3047–3061.

[39] Kim, J.; Jozic, A.; Lin, Y. X.; Eygeris, Y.; Bloom, E.; Tan, X. C.; Acosta, C.; MacDonald, K. D.; Welsher, K. D.; Sahay, G. Engineering lipid nanoparticles for enhanced intracellular delivery of mRNA through inhalation. *ACS Nano* **2022**, *16*, 14792–14806.

[40] Osman, G.; Rodriguez, J.; Chan, S. Y.; Chisholm, J.; Duncan, G.; Kim, N.; Tatler, A. L.; Shakesheff, K. M.; Hanes, J.; Suk, J. S. et al. PEGylated enhanced cell penetrating peptide nanoparticles for lung gene therapy. *J. Control. Release* **2018**, *285*, 35–45.